Covariations between the Indian Ocean dipole and ENSO: a modeling study

Hui Wang[1], Arun Kumar[1], Raghu Murtugudde[2], Balachandrudu Narapusetty[1,2,3], Knut L. Seip[4]

[1] NOAA/NWS/NCEP/Climate Prediction Center, College Park, Maryland, USA

[2] ESSIC, University of Maryland, College Park, Maryland, USA

[3] Innovim, Greenbelt, Maryland, USA

[4] Faculty of Technology, Art, and Design, OsloMet – Oslo Metropolitan University, Oslo, Norway

Climate Dynamics

Manuscript submitted on 30 May 2018 and revised on 26 April 2019 and 21 June 2019

Corresponding author address:

Hui Wang, NOAA Climate Prediction Center, 5830 University Research Court, NCWCP, College Park, MD 20740, USA

e-mail: hui.wang@noaa.gov

Abstract

The coevolution of the Indian Ocean dipole (IOD) and El Niño-Southern Oscillation (ENSO) is examined using both observational data and coupled global climate model simulations. The covariability of IOD and ENSO is analyzed by applying the extended empirical orthogonal function (EEOF) method to the surface and subsurface ocean temperatures in the tropical Indian Ocean and western Pacific. The first EEOF mode shows the evolution of IOD that lags ENSO, whereas the second mode exhibits the transition from a dipole mode to a basin-wide mode in the tropical Indian Ocean that leads ENSO. The lead-lag relationships between IOD and ENSO are consistent with two-way interactions between them. A comparison between two 500-year model simulations with and without ENSO shows that ENSO can enhance the variability of IOD at interannual time scale. The influence of ENSO on the IOD intensity is larger for the eastern pole than for the western pole, and further, is stronger in the negative IOD phase than in the positive phase. The influence of IOD on ENSO is demonstrated by the improvement of ENSO prediction using sea surface temperature (SST) in the tropical Indian Ocean as an ENSO precursor. The improvement of the ENSO forecast skill is found at both a short lead time (0 month) and long leads (10–15 months). The SST in the western pole has more predictive value than in the eastern pole. The eastward propagation of surface and subsurface temperature signals from the western Indian Ocean that precedes the development of heat content anomaly in the tropical western Pacific is the key for extending the lead time for ENSO prediction. Our results are consistent with previously reported findings but highlight the spatial-temporal evolution of the ENSO-IOD system. It is also illustrated that IOD would have been more helpful in predicting the 1997/98 El Niño than the 2015/16 El Niño.

Keywords Indian Ocean dipole, El Niño-Southern Oscillation (ENSO), Climate modeling

1. Introduction

The Indian Ocean dipole (IOD) is an intrinsic mode of variability of the tropical Indian Ocean (Saji et al. 1999; Webster et al. 1999; Murtugudde et al. 2000; Ashok et al. 2003a; Behera et al. 2006; Luo et al. 2008, 2010; Du et al. 2013; Wang et al. 2016; Saji 2018). It has broad impacts on regional climate (e.g., Ashok et al. 2001, 2003b, 2004; Annamalai and Murtugudde 2004; Li and Mu 2001; Xiao et al. 2002; Saji and Yamagata 2003a; Behera et al. 2005; Tamura et al. 2011; Cherchi and Navarra 2013). An important issue in the studies of IOD is the relationship between IOD and the El Niño-Southern Oscillation (ENSO). Previous studies have shown that the development of IOD can be independent of ENSO, but ENSO may also exert significant influence (Saji et al. 1999; Webster et al. 1999; Allan et al. 2001; Annamalai et al. 2003; Wang et al. 2004; Drbohlav et al. 2007; Stuecker et al. 2017). In recent years, it has also been found that IOD can affect ENSO (Izumo et al. 2010, 2014, 2016; Zhou et al. 2015; Jourdain et al. 2016). Clearly, there exist two-way interactions between IOD and ENSO.

Figure 1 shows the spatial distribution of seasonal mean sea surface temperature (SST) anomaly in September, October, and November (SON) of 1997 and 2015, which is the peak season of the IOD life cycle. In the eastern equatorial Pacific, SST anomalies were observed well above 3 K even before the winter season in both years, leading to descriptors like Super El Niños. In the meantime, there was a dipole in the tropical Indian Ocean, with warm SST anomalies in the western Indian Ocean (WIO) and cold anomalies in the eastern Indian Ocean (EIO). Noticeably, both El Niño events were accompanied by an IOD in its positive phase although IOD was relatively weak during 2015, where the IOD index (e.g., Saji et al. 1999) is defined as the difference between SST anomalies averaged over the WIO (50^{o}–70^{o}E, 10^{o}S–10^{o}N) and EIO (90^{o}–110^{o}E, 10^{o}S–Eq.).

Although a positive (negative) IOD tends to co-occur with El Niño (La Niña) as shown in Fig. 1, which is also found in previous studies (e.g., Annamalai et al. 2003; Behera et al. 2006; Luo et al. 2010), the spatial-temporal covariations of the two major climate modes in the tropical Pacific and Indian Oceans have not been well documented; particularly, in terms of their two-way interactions. Several studies have demonstrated that the state of IOD may help predict the following year's ENSO, and thus extend the forecast lead time to longer than a year (Wu and Kirtman 2004; Annamalai 2005; Izumo et al. 2010; Dayan et al. 2014; Jourdain et al. 2016). It would be interesting to know whether IOD can help predict a major El Niño like the 1997/98 and 2015/16 events at a lead time longer than current operational seasonal forecasts (9–10 months). It would also be interesting to know the relative importance of the eastern and western poles to the ENSO prediction.

A recent modeling study by Wang et al. (2016) proposed a forcing mechanism for IOD in the absence of ENSO. After suppressing the ENSO-related SST variability in a coupled model and based on the analysis of a 500-year simulation, they showed that the SST anomaly in EIO associated with IOD can be generated through local low-level wind response to springtime Indonesian rainfall anomaly. The time evolution of IOD without ENSO, together with the associated tropical Indian Ocean subsurface variability was also documented.

This study is aimed at examining the evolution of IOD in the presence of ENSO. The present work complements the analysis of Wang et al. (2016) by analyzing the spatial-temporal covariations between IOD and ENSO, characterizing lead and lag relationships between them, and quantifying the influence of ENSO. This is achieved by analyzing a 500-year long fully coupled model simulation, which retains the ENSO mode of variability (referred to as ENSO run hereafter), and comparing the results with the 500-year simulation in which the ENSO mode is

suppressed (referred to as no-ENSO run hereafter). The latter was analyzed and presented in Wang et al. (2016) to investigate the forcing mechanism and to characterize the spatial-temporal evolution of IOD in the absence of ENSO. The differences in the characteristics of IOD between the two simulations quantify the impact of ENSO on IOD.

This paper is organized as follows. Section 2 provides brief descriptions of the data, model, and experimental design. The coevolution between IOD and ENSO is examined in Section 3, including both the impact of ENSO on IOD and the influence of IOD on ENSO prediction. Conclusions are presented in Section 4.

2. Data, model and experimental design

The data used in this study consist of precipitation, SST, subsurface ocean temperature, warm water volume (WWV), and 10-m wind. They are taken from observations (including reanalysis data) and model simulations. Observational SSTs are obtained from the National Oceanic and Atmospheric Administration (NOAA) Optimum Interpolation SST version 2 (OISSTv2; Reynolds et al. 2002) on a $1^o \times 1^o$ (latitude × longitude) grid. The WWV is defined as the volume of water warmer than 20°C in the tropical Pacific (120°E–80°W, 5°S–5°N) and derived based on ocean temperature profiles from TAO moorings (Meinen and McPhaden 2000; data available at http://www.pmel.noaa.gov/tao/wwv/data/wwv.dat). Both SST and WWV data are monthly means from 1982 to 2016. The subsurface ocean temperatures are taken from an ocean reanalysis dataset, namely, the National Centers for Environmental Prediction's (NCEP) Global Ocean Data Assimilation System (GODAS; Behringer and Xue 2004). GODAS has a horizontal resolution of $0.333^o \times 1^o$ (latitude × longitude) and 40 layers from 5 m below sea level to 4478 m depth with 20 layers in the upper 200 m. The GODAS dataset covers a 36-year period from 1980 to 2015.

To assess the impact of ENSO on IOD, we analyze and compare two 500-year simulations with and without the ENSO mode, similar to Behera et al. (2006). The simulations were conducted with the NCEP Climate Forecast System version 1 (CFSv1; Saha et al. 2006). The coupled model consists of atmosphere, ocean, and land components. They are the NCEP Global Forecast System (GFS) version 1 (Moorthi et al. 2001), the Geophysical Fluid Dynamics Laboratory (GFDL) Modular Ocean Model version 3 (MOM3; Pacanowski and Griffies 1998), and the Oregon State University (OSU) land surface model (LSM; Pan and Mahrt 1987), respectively. The atmospheric model has T62 horizontal resolution and 64 vertical levels. The ocean model covers global oceans from 74°S to 64°N with a zonal resolution of 1° and meridional resolutions of 1/3° in the tropics (10°S–10°N) and decreasing to 1° in the extratropics (poleward of 30°S and 30°N). It has 40 vertical layers, same as GODAS. More detailed descriptions of the CFSv1 were given by Saha et al. (2006).

For both the ENSO run and no-ENSO run, the CFSv1 was integrated for 500 years. The ENSO run is a fully coupled simulation which allows air-sea interaction and retains the ENSO mode of variability. In the no-ENSO run, ENSO is suppressed by nudging the model daily SST (SST_{MOM3}) to an observed daily SST climatology (SST_{OBS}) in the tropical Pacific (140°E–75°W, 10°S–10°N). The resultant new SST (SST_{NEW}) is

$$SST_{NEW} = (1 - w) \times SST_{MOM3} + w \times SST_{OBS},$$

where w is a weighting coefficient, which is 1/3 in the domain of (140°E–75°W, 10°S–10°N) and is linearly reduced to 0 on the border of a larger domain (130°E–65°W, 15°S–15°N). The daily SST climatology was interpolated from the long-term mean (1981–2008) monthly SST of the NOAA OISSTv2 (Reynolds et al. 2002) dataset. Using w = 1/3, the model SST is relaxed to the observed climatology with an e-folding time of 3.3 days, which effectively removes the

interannual variability of SST in the tropical Pacific and El Niño/La Niña as well. This set of two 500-year simulations has been employed for the studies of the ENSO diversity (Kim et al. 2012), the Pacific decadal oscillation (Wang et al. 2012a, 2012b; Kumar et al. 2013), the IOD (Wang et al. 2016), decadal predictability (Kumar and Wang 2015), and the impact of ENSO on droughts in the Southwest U.S. (Wang and Kumar 2015) and East China (Liu et al. 2017).

The results presented in this study are based on the analysis of the last 480 years of the ENSO run and no-ENSO run. As shown by Wang et al. (2016), in the absence of ENSO, the IOD in the no-ENSO run possesses some of the fundamental features of the observed IOD. Therefore, the differences in the characteristics of IOD between the two simulations may indicate the impact of ENSO on IOD.

3. Results

3.1 Covariations between IOD and ENSO

The spatial-temporal covariations between IOD and ENSO are examined first by using the extended empirical orthogonal function (EEOF) method (Weare and Nasstrom 1982). The EEOF analysis is based on the spatial-temporal covariance matrix of 480-year monthly mean ocean temperature averaged between 10^{o}S and 5^{o}N to represent tropical ocean temperature variability with a temporal window of 18 months. The longitude–depth domain for the EEOF analysis is from 50^{o}E to 180^{o}, covering the tropical Indian Ocean and western Pacific, and from 5-m to 225-m depth below the sea surface, thus including both sea surface (5-m depth, the top layer of the ocean model) and subsurface. Unlike ordinary EOFs in which spatially propagating signals need to be described by a pair of EOF modes (e.g., Wang et al. 2013), single EEOF mode can represent propagating features (Weare and Nasstrom 1982).

Figure 2 shows the first EEOF mode (EEOF1) in the form of correlation and regression maps for ocean temperature averaged between 10°S and 5°N from month 0 to month 28. These maps are obtained by correlating and regressing the ocean temperature anomalies against the principal component (PC) time series of EEOF1 for ocean temperature lagging PC1 by 0 month to 28 months. This mode accounts for 31% of surface and subsurface temperature variance in the tropical Indian Ocean and western Pacific.

The time evolution of EEOF1 begins with warm subsurface temperature anomalies in the tropical western Pacific (Fig. 2, month 0). From month 2 to 4, temperature anomalies propagate eastward along the thermocline, generate warm SST anomalies in the eastern and central Pacific, and result in coupled Bjerknes feedback (Bjerknes 1969) and hence an El Niño. In the following months (Fig. 2, months 6–14), the El Niño continues to grow with increases in SST and subsurface temperature anomalies. In the meantime, cold temperature anomalies develop in the tropical western Pacific, as well as in EIO while warm anomalies develop in WIO. The latter two form a positive IOD.

During the decay phase of the El Niño (Fig. 2, months 18–26), warm temperature anomalies in WIO propagate eastward and replace cold anomalies in EIO. As a consequence, a basin-wide warming takes place in both the surface and subsurface tropical Indian Ocean, consistent with the tropical Indian Ocean surface and subsurface responses to El Niño (e.g., Cadet 1985; Klein et al. 1999; Wang et al. 2013). In month 28, EEOF1 ends up with warm temperature anomalies in EIO and cold subsurface temperature anomalies in the western Pacific. The latter favors the development of a La Niña. Figure 2 illustrates that the development of a positive IOD and its transition to a basin-wide warming in the tropical Indian Ocean lag the El Niño.

182 The second EEOF (EEOF2) is shown in Fig. 3, which accounts for 16% of the surface
183 and subsurface temperature variance. In month 0, there is an El Niño in the tropical Pacific and a
184 positive IOD in the tropical Indian Ocean. Although the magnitudes of the associated
185 temperature anomalies are relatively small (Fig. 3, months 0–10), their spatial structures are like
186 those in EEOF1 (Fig. 2, months 10–20). Also, similar to EEOF1 (Fig. 2, months 18–26), the
187 decay of the El Niño in EEOF2 is associated with the thermocline variability in the tropical
188 Pacific and eastward propagating temperature anomalies in the tropical Indian Ocean, leading to
189 a basin-wide mode (Fig. 3, months 8–16). In month 18 (Fig. 3), the tropical Pacific is
190 characterized by a La Niña with cold temperature anomalies in both the surface and subsurface,
191 whereas EIO is dominated by warm anomalies. In the following months, cold anomalies develop
192 in WIO, leading to a negative IOD. Additionally, there are weak warm anomalies in the western
193 Pacific in month 20. These warm anomalies continue to intensify during months 22–28, shift
194 eastward, and are precursors for the next El Niño. The warm anomalies in the surface and
195 subsurface of the western Pacific come after the warm anomalies in EIO originating from WIO.
196 This suggests that both the IOD and the following basin-wide mode lead the forthcoming El
197 Niño. In month 28 (Fig. 3), the distributions of temperature anomalies in the two tropical basins
198 are out of phase with those in month 0. Figure 3 thus displays a half cycle of the evolutions of
199 IOD and El Niño/La Niña associated with EEOF2.

200 The two leading EEOF modes capture the covariations between IOD and ENSO that are
201 associated with tropical ocean subsurface variability. In both modes, there are strong links
202 between surface and subsurface temperature anomalies. Each mode represents a distinctive
203 relationship between IOD and ENSO. In the first mode, a positive IOD lags an El Niño. In the
204 second mode, a positive IOD and a basin-wide mode lead the development of warm ocean

temperature anomalies in the western Pacific, a precursor for El Niño. Similar lead and lag relationships between IOD and ENSO are also obtained by the EEOF analysis with the 36-year GODAS data (not shown).

The spatial-temporal covariations and the lead-lag relationships between IOD and ENSO depicted by the two EEOFs can also be seen in the SST field. Figures 4 and 5 show the evolution of the SST anomalies associated with EEOF1 and EEOF2, respectively, together with the 10-m wind and precipitation anomalies obtained by regressing the 480-year monthly mean data against the PC1 and PC2 time series. Associated with EEOF1, the development of El Niño (Fig. 4, month 4) precedes the negative precipitation anomalies in Indonesia (month 6) and the easterly and southeasterly wind anomalies in EIO (months 6 and 8), which trigger the onset of IOD (months 8 and 10; Annamalai et al. 2003; Hendon 2003; Wang et al. 2016). The surface wind anomalies (Fig. 4, months 6–12) are a response to dry conditions across Indonesia induced by El Niño through a weakened Walker circulation (Hendon 2003). The basin-wide warming in the tropical Indian Ocean (Fig. 4, months 18–22) is also a response to El Niño (e.g., Latif and Barnett 1995; Wallace et al. 1998; Saji and Yamagata 2003b; Okumura and Deser 2010; Xie et al. 2009). Therefore, EEOF1 reflects the IOD response to ENSO.

In EEOF2, the warm SST anomalies associated with the basin-wide mode move eastward in the tropical Indian Ocean, leading to a reversal in zonal wind over the equatorial Indian Ocean (Fig. 5, months 10–16). Together with the easterly wind anomalies in the western Pacific associated with La Niña, they produce low-level wind convergence and cause positive precipitation anomalies over the Indo-Pacific warm pool (Fig. 5, months 16–20). Warm water also piles up in the same region, which increases SST and deepens the thermocline in the western Pacific (Figs. 3 and 5, months 20–24). The eastward movement of the subsurface warm

temperature anomalies from the western Pacific (Fig. 3, month 24–28) is a precursor of an El Niño. It is indeed observed that the development of an El Niño may follow a basin-wide warming in the tropical Indian Ocean (Wu and Kirtman 2004; Annamalai et al. 2005). The second EEOF thus indicates an influence of the tropical Indian Ocean on the western Pacific. The two EEOF modes portray the combined evolution of IOD and El Niño/La Niña together as a coupled system. It is suggested that the IOD and the basin-wide warming in the tropical Indian Ocean may be a response to El Niño, which in turn may help the development of El Niño. Figures 4 and 5 also indicate that the atmospheric circulation links the changes in SST in the two ocean basins. Their two-way interactions are further examined in the following two subsections.

3.2 Impact of ENSO on IOD

3.2.1 Frequency

Based on the analysis of IOD in the no-ENSO run, Wang et al. (2016) demonstrated that ENSO is not fundamental for the existence of IOD. In the absence of ENSO, IOD can be initiated by springtime Indonesian precipitation anomalies through the surface wind response over EIO. To characterize the variability of Indonesian precipitation, Hendon (2003) defined an Indonesian precipitation (IndoP) index by averaging precipitation anomalies over the maritime continent within the domain of (95°E–141°E, 10°S–5°N). The onset of IOD triggered by IndoP was supported by the lagged relationship between spring IndoP and the IOD-related 10-m wind/SST of the following summer and fall (Wang et al. 2016, their Fig. 5). *Given a strong influence of ENSO on Indonesian precipitation (Hendon 2003), IndoP may further act as a medium linking IOD and ENSO.*

Figure 6a shows the power spectra of the IndoP index in both the ENSO run and no-ENSO run, as well as the Niño 3.4 SST index in the ENSO run. To obtain smoothed power

spectra, the 480-year time series is divided into eight segments of 60 years. The power spectra shown in Fig. 6 are an average of the spectra computed for the eight individual segments. The statistical significance of spectral peaks is estimated by comparing these peaks to corresponding red-noise spectra.

The power spectrum of the Niño 3.4 index in the ENSO run is characterized by significant peaks at the interannual time scale between 2.5 and 6.5 years. The IndoP in the ENSO run also displays significant peaks at the interannual time scale between 3 and 6 years, consistent with the ENSO forcing. In contrast, the IndoP in the no-ENSO run lacks power at the interannual time scale presumably due to the absence of ENSO in the simulation. Additionally, the IndoP index in both the ENSO run and no-ENSO run shows significant peaks at short time scales (< 2.5 years), which are likely independent of ENSO. Figure 6b shows the power spectra of the IOD index in both the ENSO and no-ENSO runs. The most significant difference between the two is the spectral peak at 4 years in the ENSO run, indicating enhanced IOD variability at interannual time scale by ENSO.

The power spectrum analysis is also applied to the PC time series of EEOF1 and EEOF2 in both the ENSO and no-ENSO runs (Fig. 7). In the ENSO run (Fig. 7a), both EEOF1 and EEOF2 are dominated by the variability at interannual time scale. The spectral peaks are at 5.5 and 4 years for EEOF1 and EEOF2, respectively, which are close to the largest peaks of the Niño 3.4 index (5 years) and the IOD index (4 years, Fig. 6b, red). In the no-ENSO run (Fig. 7b), both EEOF modes (their spatial patterns shown in Figs. 11 and 12 in Wang et al. 2016) are characterized by the spectral peaks at shorter time scales ranging from 1 year to 4 years, consistent with those of the IOD index in the no-ENSO run (Fig. 6b, blue). The power in these spectral peaks (Fig. 7b) is weaker than those in the ENSO run (Fig. 7a).

A comparison between Fig. 7a and 7b reveals that in the absence of ENSO, the variability of IOD, which is represented by the two leading EEOFs in the no-ENSO run (Wang et al. 2016), is confined to a relatively shorter time scale (< 4 years). In the presence of ENSO, there is strong covariability between IOD and ENSO at the interannual time scale. Therefore, the variability of IOD is also significantly enhanced at interannual time scale. The result is consistent with the power spectrum of the IOD index in the ENSO run (Fig. 6b, red).

Whether the results based on the model simulations are reliable is further assessed by comparing the power spectra of the Niño 3.4 index, the IOD index, and the two PC time series in the ENSO run (Figs. 6b, 7a) to those derived from the 36-year GODAS data shown in Fig. 8. Overall, the spectral peaks of these time series in the ENSO run are like those in GODAS. This similarity gives us confidence for evaluating the ENSO influence on IOD with the two simulations. It is also noted that the power spectra of the IOD in GODAS show a minimum power at 2 years (Fig. 8a), which is different from the quasi-biennial variation of the IOD found in previous studies (e.g., Saji et al. 1999). To ascertain the power peaks of IOD from the GODAS analysis, a similar analysis is performed on the IOD index derived from the OISST dataset. The corresponding power spectra (not shown) are very similar to those in Fig. 8a, also with a minimum at 2 years. More discussions on this issue are presented in the Appendix.

3.2.2 Time evolution

As shown in Figs. 2 and 3, the time evolution of EEOF1 from month 12 to month 28 is like that of EEOF2 from month 0 to month 16. This suggests that the covariations between IOD and ENSO involve an alternation between the two EEOF modes. The simultaneous correlation between the two PC time series is zero because of the constraint of orthogonality for the EEOF

296 method. However, the lead-lag correlations between the two PCs are nonzero. Figure 9a shows
297 such lead-lag correlations in both the ENSO run and no-ENSO run, as well as in GODAS.

298 For the ENSO run (red solid line), the largest positive (negative) correlation is found
299 when PC1 leads (lags) PC2 by about 11 months. For example, the evolution of IOD and ENSO
300 is first dominated by EEOF1 (Fig. 2). A positive IOD follows an El Niño during the developing
301 phase (Fig. 2, months 0–12). When the El Niño reaches its peak intensity in month 14 (Fig. 2),
302 EEOF2 may kick in (Fig. 3) between months 2 and 4 because of the largest positive correlation
303 with an 11-month lag. The covariation of IOD and ENSO continues in the following 22 months
304 (Fig. 3), including the decay of the El Niño from month 4 to month 14 and the development of a
305 La Niña from month 16 to month 24. In the meantime, there is a transition from a positive IOD
306 to a basin-wide warming in the Indian Ocean during month 4 and month 16, followed by a
307 negative IOD from month 18 to month 24 and the warming of the western Pacific subsurface
308 during months 20 and 24. After the 22-month evolution, both IOD and ENSO (Fig. 3, month 26)
309 are opposite to their initial phase when EEOF2 gets started (Fig. 3, month 4). They may
310 continue to evolve and return to EEOF1 (Fig. 2) in month 15 because of the largest negative
311 correlation with an 11-month lag. The conceptual picture of the covariations of ENSO and IOD
312 through the alternation between EEOF1 and EEOF2 is summarized in Fig. 10.

313 The time interval between the two vertical dashed red lines in Fig. 9a is an estimation of
314 the timescale (11 + 11 = 22 months) for an alternation between the two modes. It also
315 characterizes the timescale of the covariations between IOD and ENSO. This timescale in the
316 ENSO run (22 months) is comparable to the observations (GODAS, 9 + 9 = 18 months), but is
317 longer than that in the no-ENSO run (7 + 5 = 12 months). The difference in the timescale

between the ENSO run and no-ENSO run is another indicator of the influence of ENSO on the evolution of IOD.

The covariations of IOD and ENSO via the alternation between the two EEOFs can also be seen in the lead and lag correlations of the Niño 3.4 and IOD indices with the two PC time series of EEOF1 and EEOF2 in the ENSO run, as shown in Fig. 9b. Both the indices correlate with EEOF1 with a maximum correlation when EEOF1 leads the indices by 4 months (orange and blue). The lead and lag correlations of the two indices with EEOF2 (yellow and green) are similar to the lead and lag correlations between EEOF1 and EEOF2 (Fig. 9a, red), with a maximum correlation (positive) when the indices lead EEOF2 and a minimum (negative) when the two indices lag EEOF2. Compared to the correlations of EEOF1 with EEOF2 in Fig. 9a (red), the maxima and minima in Fig. 9b (yellow and green) shift towards right, consistent with the maximum correlations between EEOF1 and the two indices at a 4-month lag (Fig. 9b, orange and blue). The positive maximum and negative minimum correlations with EEOF2 indicate that the phase change for both ENSO and IOD can happen during the evolution of EEOF2 (Fig. 3). The half-cycle time is around 20 months for ENSO and 14 months for IOD, estimated based on the lag interval between the positive and negative extreme correlations, which is consistent with the relatively low-frequency variability of ENSO and higher-frequency variability of IOD (Fig. 6b). It is also obvious that the lead and lag correlations of the Niño 3.4 index with the two PC time series are much stronger than those of the IOD index with the two PCs. The lead and lag correlations between the two indices (Fig. 9b, red) show a maximum of 0.28 when the IOD index leads the Nino 3.4 index by 1 month, suggesting a certain chance of co-occurrence of ENSO and IOD (e.g., Fig. 1).

340 The co-occurrence of IOD and ENSO is further examined in Table 1 by counting the
341 number of SON seasons during which a positive (negative) IOD co-occurs with an El Niño (La
342 Niña) in the 480-year simulations. Both the ENSO and IOD events are defined with their index
343 value that exceeds their corresponding one standard deviation. In the model simulations, the
344 standard deviations of the 480-year SON Niño 3.4 index and the IOD time series are 0.90 K and
345 1.20 K, respectively. There are 79 El Niño and 88 La Niña events and 108 positive and 90
346 negative IOD events. Among them, 29 (35) SON seasons are found with the co-occurrence of a
347 positive (negative) IOD and an El Niño (La Niña), which accounts for 27% and 39% of positive
348 and negative IOD events, respectively. It is also found that 5% of positive IODs and 4% of
349 negative IODs in the model co-occur with La Niña and El Niño, respectively. Such IOD–ENSO
350 combinations also exist in observations (e.g., Saji et al. 1999, their Fig. 1).

351 *3.2.3 Intensity*

352 ENSO not only influences the temporal scale of IOD, but also affects the intensity of
353 IOD. Figure 11 shows the scatter plot of EIO SST anomaly versus WIO SST anomaly in SON,
354 the peak season of IOD, for both the ENSO and no-ENSO runs. It is evident that the amplitudes
355 of these SST anomalies are larger in Fig. 11b than in Fig. 11a, especially in the right lower
356 quadrant during the negative IOD phase. Compared to the no-ENSO run, the SST variance in
357 the ENSO run is increased by 42% and 25%, respectively, in the eastern and western poles of
358 IOD. The variance of the IOD index is increased by 30%. The corresponding increases are 14%
359 (eastern pole), 2% (western pole), and 6% (dipole) when IOD is in a positive phase. In contrast,
360 they are 55%, 50%, and 52% when IOD is in a negative phase. Therefore, the ENSO impact on
361 the IOD intensity is larger for the eastern pole than for the western pole, and is stronger during a
362 negative IOD event than during a positive event. This is consistent with the fact that there is also

363 an east-west asymmetry in the ocean dynamics with a stronger mixed layer-thermocline
364 interaction in the eastern pole than in the western pole (Murtugudde and Busalacchi 1999,
365 Murtugudde et al. 2000). The results, therefore, reveal an asymmetry of the ENSO influence
366 between the positive and negative IOD phases.

367 **3.3 Influence of IOD on ENSO prediction**

368 The impact of IOD on ENSO can be manifested in its influence on the skill of ENSO
369 prediction. Figure 3 illustrates that the evolution of EEOF2 involves eastward propagation of
370 warm temperature anomalies from WIO, followed by the development of warm subsurface
371 temperature anomalies in the western tropical Pacific which in turn leads to an El Niño. The
372 lagged relationship provides a basis for using SST anomaly in WIO as a predictor for ENSO
373 forecast. To demonstrate the feasibility of this hypothesis, a linear regression model is employed
374 to statistically forecast winter seasonal mean (December, January, and February, DJF) Niño 3.4
375 SST. The forecasts are cross-validated and compared with similar statistical forecasts using
376 WWV as a predictor, as well as the CFSv2 dynamical seasonal forecasts (Saha et al. 2014).

377 Figure 12 shows the forecast skills assessed by anomaly correlations between the
378 predicted and observed Niño 3.4 SST over 1983–2010, the CFSv2 hindcast period (Saha et al.
379 2014), for the statistical forecasts using WIO SST and WWV as predictors and the CFSv2
380 retrospective forecasts (Saha et al. 2014). Both predictors, namely, WIO SST and WWV, are
381 derived from pre-season observations. The former is the average of SSTs over the WIO domain
382 (50^{o}–70^{o}E, 10^{o}S–10^{o}N) and the latter is the volume of water warmer than 20^{o}C in the equatorial
383 Pacific (120^{o}E–80^{o}W, 5^{o}S–5^{o}N), which is a proxy for the thermocline depth and subsurface heat
384 content (Meinen and McPhaden 2000). To predict DJF Niño 3.4 SST, WIO SST and WWV of
385 each month from the January of previous year to the November of current year (Fig. 12, x-axis

386 labels) are used as an input for the linear-regression forecast model, corresponding to lead times
387 from 22 months to 0 month (Fig. 12, x-axis labels). The CFSv2 only provides 9-month lead
388 forecasts, resulting in the DJF Niño 3.4 SST forecasts with lead times from 6 months (initialized
389 in May) to 0 month (initialized in November).

390 The CFSv2 has the highest forecast skill at all available lead times (0–6 months) with all
391 anomaly correlations above 0.7 (Fig. 12, black line). The skill of the statistical forecasts based
392 on WWV (purple line) is lower than the dynamical forecasts, but the anomaly correlations are
393 above the 99% significance level (0.48, solid gray line) at 0- to 10-month leads. There is a sharp
394 decrease in the anomaly correlation at the 12-month lead, beyond which no skillful forecasts are
395 found. The maximum lead of 12 months is likely determined by the time needed for subsurface
396 temperature anomalies from the tropical western Pacific to cross the Pacific basin and reach the
397 sea surface in the tropical eastern Pacific. When using the WIO SST as a predictor (red line),
398 skillful forecasts are found at either a short lead time of 0 month (above the 99% significance
399 level) or longer leads of 12–16 months (above the 95% significance level). The former is
400 associated with the co-occurrence of IOD and ENSO (e.g., Fig. 1; Behera et al. 2006; Luo et al.
401 2010), whereas the latter is attributed to the signal of warm WIO SST anomalies appearing well
402 ahead (> 1 year) of El Niño (Fig. 3). The skill of the WIO SST-based forecasts is lower than
403 those of the CFSv2 and the WWV-based forecasts, but the lead time of skillful forecasts with the
404 WIO SST is longer than the other two.

405 When using both WIO SST and WWV as predictors with a multiple linear regression
406 model, the forecast skill (Fig. 12, green line) is comparable to that based solely on WWV (purple
407 line) at lead times from 0 to 10 months, but is significantly improved at longer leads. For
408 instance, the anomaly correlation skills of the WWV-based forecasts (purple line) are 0.50 and

409 0.10 at the 10-month and 13-month leads, respectively. The corresponding skills with the two
410 predictors (green line) are 0.57 and 0.52. The results presented in Fig. 12 suggest that for the
411 ENSO prediction, the statistical forecast based on WWV can extend the limit of lead time of the
412 dynamical forecast from 6 months to 10 months. Using the WIO SST as an additional predictor
413 can further extend the lead times of skillful forecasts up to 13 months (99% significance level) or
414 15 months (95% significance level). This is consistent with the findings of Wieners et al. (2016)
415 that WIO may affect ENSO and an El Nino is preceded by the change in WIO SST about 15
416 month earlier.

417 Figure 12 also presents the forecast skills using the EIO SST and the IOD index as
418 individual predictors. Comparing to the forecast skill with the WIO SST (red line), the skill with
419 the EIO SST (yellow line) is slightly better at short leads, but much worse at long leads.
420 Consistently, the skill with the IOD index (orange line), consisting of both the EIO and WIO
421 SSTs is relatively high at short lead times, and degraded at long leads due to the EIO SST. As a
422 result, the forecast skill is not significantly improved when adding the EIO SST to WWV at long
423 leads (cyan line vs. purple line). The skill with WWV and IOD (blue line) is also not as good as
424 that with WWV and WIO (green line) at long leads. Clearly, the improvement of ENSO
425 prediction at long leads (10–15 months) is attributable to the WIO SST.

426 How the WIO SST contributes to the ENSO prediction is further examined for the two
427 big El Niño events (1997/98 and 2015/16). Figure 13 shows the predicted Niño 3.4 SST
428 anomalies for DJF 1997/98 and 2015/16 with the linear regression model using both individual
429 predictors (WWV, WIO SST) and two predictors (WWV + WIO SST) at lead times from 22
430 months to 0 month. The observed values of the Niño 3.4 index are 2.50 K and 2.56 K for DJF
431 1997/98 and DJF 2015/16, respectively. All forecasts with a maximum value of 1.7 K in Fig. 13

are weaker than the observed. If El Niño is defined by the Niño 3.4 index with a threshold of 0.5 K (e.g., Trenberth 1997), the 1997/98 and 2015/16 events could be predicted at lead times of 11 and 10 months, respectively, using WWV as the predictor (Fig. 13, blue bars). Adding the WIO SST as an extra predictor extends the maximum lead time for forecasting El Niño to 16 and 11 months (Fig. 13, green bars), respectively, for the two events. Additionally, the WIO SST helps ENSO prediction not only at long leads, but also at short leads (0–2 months) by increasing the magnitude of the predicted Niño 3.4 index (Fig. 13, red and green bars). This is consistent with the overall forecast skill assessed by the cross-validations (Fig. 12, red line). Figure 13 also suggests that the WIO SST improves the ENSO prediction more significantly for the 1997/98 El Niño than for the 2015/16 El Niño, especially at long lead times (11–16 months). The difference may be due to their different lead-lag relationships with IOD or the difference in the strength of the IOD itself. For the 1997/98 event, the projection of surface and subsurface ocean temperatures onto EEOF2 (–2.45) is more than onto EEOF1 (1.83), whereas for the 2015/16 events, the projection onto EEOF1 (1.36) is more than onto EEOF2 (–1.14), based on the EEOF analysis of the GODAS data (not shown). Indeed, a recent study by Mayer et al. (2018) discloses different energetics of the 1997/98 and 2015/16 El Nino events in relation to the Indian Ocean.

Possible mechanisms responsible for the influence of IOD on ENSO have been discussed in some previous studies via both the atmospheric bridge and oceanic pathway (e.g., Wijffels and Meyers 2004; Annamalai et al. 2005; Izumo et al. 2010; Wieners et al. 2016). The atmospheric processes involve changes in the low-level zonal wind over the equatorial Pacific through the Walker Circulation or via the Philippine Sea anticyclone. More specifically, warm SST anomaly in WIO enhances local convection, which leads to suppressed convection over Indonesia and a

455 weakened Walker Circulation over the tropical Pacific sector. Alternatively, perturbations to the
456 Philippine Sea anticyclone generate a Kelvin wave which can also alter the western Pacific
457 circulation. Both processes are invoked as modulators of the surface zonal wind in the tropical
458 Pacific and thus capable of affecting the development of ENSO.

459 **4. Conclusions and discussions**

460 In this study the coevolution of IOD and ENSO is assessed by analyzing and comparing
461 two 500-year CFS coupled model simulations with and without ENSO. The EEOF analysis of
462 surface and subsurface ocean temperatures in the tropical Indian Ocean and western Pacific from
463 the ENSO run reveals strong covariability of IOD and ENSO that are closely related to the
464 subsurface ocean variability across the two tropical ocean sectors. The first EEOF mode shows
465 the development of a positive IOD that lags El Niño, while the second mode exhibits the
466 transition from a positive IOD to a basin-wide warming that leads El Niño. The lead and lag
467 relationships between IOD and ENSO are consistent with two-way interactions between them.

468 The impact of ENSO on IOD was examined through a comparison between the ENSO
469 and no-ENSO runs. The results indicate that ENSO not only enhances the variability of IOD at
470 the interannual time scale but also increases the amplitude of SST anomalies in the IOD regions.
471 A further comparison between the SST variances in the regions of EIO and WIO discloses the
472 asymmetries of the ENSO influence between the eastern and western poles and between the
473 positive and negative IOD phases. Specifically, the influence of ENSO on the IOD intensity is
474 larger for the eastern pole than for the western pole, and is stronger in a negative IOD phase than
475 in a positive phase.

476 The impact of IOD on ENSO was demonstrated by the improvement of ENSO prediction
477 when considering the WIO SST as an ENSO precursor. The improvement is found not only at a

short lead time (0 month) but also at long leads (10–15 months). The WIO SST plays a much more important role than the EIO SST in improving ENSO prediction at long leads. The eastward propagating surface and subsurface temperature signals from the western Indian Ocean that precede the development of heat content anomaly in the tropical western Pacific are the key for extending the lead time for ENSO prediction. It is also shown that WIO SST helps ENSO prediction more effectively for the 1997/98 El Niño than for the 2015/16 El Niño, which is likely due to their different lead-lag relationships with IOD and the strength of IOD between the two ENSO events.

A recent study by Saji (2018) argues that the basinwide SST anomalies in the tropical Indian Ocean induced by ENSO are zonally nonuniform. The impact of ENSO thus cannot be removed by the difference between the WIO and EIO SST anomalies in constructing the IOD index. A similar EEOF analysis was performed using the tropical ocean temperature anomalies after removing the ENSO signal by using 5-month lagged regression with the Niño 3.4 index, similar to what Saji and Yamagata (2003b) did, for the tropical Indian Ocean temperature east of 120^{o}E. The IOD signals are significantly weakened in the two leading EEOFs that covary with ENSO (not shown). The results show the importance of the ENSO impact on the IOD-ENSO association.

Therefore, it should be noted that the two-way interactions between ENSO and IOD may not be equally important and the impact of IOD on ENSO may depend on the mean state (see Annamalai et al. 2005; Chen 2010). Given that ENSO is a major source of interannual variability in the atmosphere-ocean system, its impact on IOD contributes significantly to the variability of IOD. In contrast, the impact of IOD should be less important to ENSO (Chen 2010). Additionally, based on a wavelet analysis with the 480-year PC time series of EEOF1

501 and EEOF2, the co-variability between ENSO and IOD exhibits variations on decadal timescales
502 (not shown; see Ashok et al. 2003a; Annamalai et al. 2005). Specifically, the co-variability is
503 strong in some decades, but weak in some other decades.

504 It should also be noted that the results presented in this paper are specific to the CFS
505 model alone and the EEOF method used. Therefore, there might be some limitations, depending
506 on the fidelity of the CFS in reproducing the mean IOD and ENSO, as well as their covariability.
507 Previous studies reveal that the CFS can reproduce the observed features of both the IOD and
508 ENSO reasonably well (e.g., Kim et al. 2012; Wang et al. 2016). Consistently, to some extent,
509 the covariations between the IOD and ENSO identified in the CFS simulations are similar to
510 those in GODAS.

511 The physical processes responsible for the interaction between IOD and ENSO may
512 involve the teleconnection through the atmospheric "bridge" (e.g., the Walker circulation, the
513 Philippine Sea anticyclone and Indonesian precipitation, Klein et al. 1999; Kumar and Hoerling
514 2003; Annamalai et al. 2005; Hendon 2013; Wieners et al. 2017b), the air-sea coupled
515 mechanisms and thermocline feedback (e.g., Lu et al. 2018), and/or ocean internal processes
516 (e.g., the Indonesian Throughflow, Wang et al. 2004; Zhou et al. 2015; Mayer et al. 2018).
517 Further studies will be needed to understand the ENSO and IOD events where this covariability
518 is not obvious and whether the preconditioning of the EIO may play a role in the strength of the
519 covariability (Annamalai et al. 2005). Further analysis is also needed for understanding the role
520 of these IOD-ENSO interactions on processes such as the recharge-discharge which are argued
521 to be fundamental for ENSO events (Jin 1997, Ramesh and Murtugudde 2013) and the likely
522 dependence of ENSO flavors on the role of IOD in ENSO (Capotondi et al. 2015; Wieners et al.
523 2017a) or the impact of Indian Ocean warming on the ENSO-IOD covariability (Lee et al. 2015).

Also of interest would be the Indo-Pacific Tripole framework proposed by Chen and Cane (2008) which may offer further process understanding of the relationship between the two basins. Further diagnoses of observations and the two simulations are required to understand the dynamics of the lead and lag linkages between IOD and ENSO documented in this study. It is nonetheless evident that the details of the evolution of warm and cold ENSOs and the positive and negative IODs represent advancement in the process understanding with demonstrable improvements in ENSO predictions.

Acknowledgments The authors would like to thank three anonymous reviewers and the editor for their insightful and constructive comments and suggestions.

Appendix

Quasi-biennial periodicity of the IOD

Previous studies (e.g., Saji et al. 1999) reveal that the IOD has a quasi-biennial variation. However, a near 2-year peak is not found in the power spectrum of the IOD in GODAS (Fig. 8a). Instead, there is a minimum power at 2 years, which is also different from the model results (Fig. 6b). One possibility that could cause the difference in the peaks between the model and GODAS is data sampling issue. For example, the power spectrum of the 480-year IOD index in the ENSO run (Fig. 6b, red line) is the average of the power spectra for 8 × 60 years. Figure A1 shows the individual spectrum for each 60 years, in addition to their average (red line). Among the eight members, there are large inter-member spreads in the power spectra. In particular, there is one with a peak at 2 years (green) and another one with a minimum at 2 years (blue). Given that the IOD index derived from the 36-year GODAS data has only one realization, it is

not surprising to see the difference in the peaks at some specific periods (here 2 years) between the model and GODAS.

References

Allan R, Chambers D, Drosdowsky W, Hendon H, Latif M, Nicholls N, Smith I, Stone R, Tourre Y (2001) Is there an Indian Ocean dipole, and is it independent of the El Niño-Southern Oscillation? CLIVAR Exchanges, 6:18–22

Annamalai H, Murtugudde R (2004) Role of the Indian Ocean in regional climate variability. Earth Climate: The Ocean-Atmosphere Interaction, Wang C, Xie S-P, Carton JA (eds.), AGU Geophysical Monograph 147:213–246

Annamalai H, Murtugudde R, Potemra J, Xie SP, Liu P, Wang B (2003) Coupled dynamics over the Indian Ocean: Spring initiation of the zonal mode. Dee-Sea Res II 50:2305–2330. doi:10.1016/S0967-0645(03)00058-4

Annamalai H, Xie SP, McCreary JP, Murtugudde R (2005) Impact of Indian Ocean sea surface temperature on developing El Niño. J Clim 18:302–319

Ashok K, Guan Z, Yamagata T (2001) Impact of the Indian Ocean dipole on the relationship between the Indian monsoon rainfall and ENSO. Geophys Res Lett 28:4499–4502

Ashok K, Guan Z, Yamagata T (2003a) A look at the relationship between the ENSO and the Indian Ocean dipole. J Meteor Soc Japan 81:41–56

Ashok K, Guan Z, Yamagata T (2003b) Influence of the Indian Ocean dipole on the Australian winter rainfall. Geophys Res Lett 30:1821. doi:10.1029/2003GL017926

Ashok K, Guan Z, Saji NH, Yamagata T (2004) Individual and combined influence of ENSO and the Indian Ocean dipole on the Indian summer monsoon. J Clim 17:3141–3155

Behera SK, Luo JJ, Masson S, Delecluse P, Gualdi S, Navarra A, Yamagata T (2005) Paramount impact of the Indian Ocean dipole on the East African short rains: A CGCM study. J Clim 18:4514–4530

572 Behera SK, Luo JJ, Masson S, Rao SA, Sakuma H, Yamagata T (2006) A CGCM study on the
573 interaction between IOD and ENSO. J Clim 19:1688–1705
574 Behringer DW, Xue Y (2004) Evaluation of the global ocean data assimilation system at NCEP:
575 The Pacific Ocean. Eighth Symp. on Integrated Observing and Assimilation Systems for
576 Atmosphere, Oceans, and Land Surface, Seattle, WA, Amer. Meteor. Soc. [Available
577 online at http://ams.confex.com/ams/84Annual/techprogram/paper_70720.htm]
578 Bjerknes J (1969) Atmospheric teleconnections from the equatorial Pacific. Mon Wea Rev
579 97:163–172
580 Cadet DL (1985) The Southern Oscillation over the Indian Ocean. J Climatol 5:189–212
581 Capotondi A et al. (2015) Understanding ENSO diversity. Bull Amer Meteor Soc 96:921–938
582 Chen D (2010) Indo-Pacific tripole: An intrinsic mode of tropical climate variability. Adv Geosci
583 24, Ocean Science, 18pp
584 Chen D, Cane MA (2008) El Nino prediction and predictability. J Comput Phys 227:3625–3640
585 Cherchi A, Navarra A (2013) Influence of ENSO and of the Indian Ocean dipole on the Indian
586 summer monsoon variability. Clim Dyn 41:81–103
587 Dayan H, Vialard J, Izumo T, Lengaigne M (2014) Does sea surface temperature outside the
588 tropical Pacific contribute to enhanced ENSO predictability? Clim Dyn 43:1311–1325
589 Drbohlav H-KL, Gualdi S, Navarra A (2007) A diagnostic study of the Indian Ocean dipole
590 mode in El Niño and non-El Niño years. J Clim 20:2961–2977
591 Du Y, Cai W, Wu Y (2013) A new type of the Indian Ocean dipole since the mid-1970s. J Clim
592 26:959–972
593 Hendon HH (2003) Indonesian rainfall variability: Impact of ENSO and local air–sea interaction.
594 J Clim 16:1775–1790
595 Izumo T et al (2010) Influence of the state of the Indian Ocean dipole on the following year's El
596 Nino. Nat Geosci 3:168–172
597 Izumo T, Lengaigne M, Vialard J, Luo JJ, Yamagata T, Madec G (2014) Influence of Indian
598 Ocean dipole and Pacific recharge on flowing year's El Nino: interdecadal robustness.
599 Clim Dyn 42:291–310

600 Izumo T, Vialard J, Dayan H, Lengaigne M, Suresh I (2016) A simple estimation of equatorial
601 Pacific response from windstress to untangle Indian Ocean dipole and basin influences on
602 El Niño. Clim Dyn 46:2247–2268
603 Jin F-F (1997) An equatorial ocean recharge paradigm for ENSO. Part I: Conceptual model. J
604 Atmos Sci 54:811–829
605 Jourdain NC, Lengaigne M, Vialard J, Izumo T, Gupta AS (2016) Further indights on the
606 influence of the Indian Ocean dipole on the following year's ENSO from observations
607 and CMIP5 models. J Clim 29:637–658
608 Kim ST, Yu J-Y, Kumar A, Wang H (2012) Examination of the two types of ENSO in the NCEP
609 CFS model and its extratropical associations. Mon Wea Rev 140:1908–1923
610 Klein SA, Soden BJ, Lau NC (1999) Remote sea surface temperature variations during ENSO:
611 Evidence for a tropical atmospheric bridge. J Clim 12:917–932
612 Kumar A, Hoerling MP (2003) The nature and causes for the delayed atmospheric response to El
613 Niño. J Clim 16:1391–1403
614 Kumar A, Wang H (2015) On the potential of extratropical SST anomalies for improving climate
615 prediction. Clim Dyn 44:2557–2569
616 Kumar A, Wang H, Wang W, Xue Y, Hu Z-Z (2013) Does knowing the oceanic PDO phase help
617 predict the atmospheric anomalies in subsequent months? J Clim 26:1268–1285
618 Latif M, Barnett TP (1995) Interactions of the tropical oceans. J Clim 8:952–964
619 Lee S-K, Park W, Baringer MO, Gordon AL, Huber B, Liu Y (2015) Pacific origin of the abrupt
620 increase in Indian Ocean heat content during the warming hiatus. Nature Geosci 8:445–
621 449
622 Li CY, Mu MQ (2001) Influence of the Indian Ocean dipole on atmospheric circulation and
623 climate. Adv Atmos Sci 18:831–843
624 Liu J, Wang H, Lu E, Kumar A (2017) Decadal modulation of East China winter precipitation by
625 ENSO. Clim Dyn doi:10.1007/s00382-016-3427-6
626 Lu B, Ren H-L, Scaife AA, Wu J, Dunstone N, Smith D, Wan J, Eade R, MacLachlan C, Gordon
627 M (2018) An extreme negative Indian Ocean Dipole event in 2016: dynamics and
628 predictability. Clim Dyn 51:89–100

629 Luo JJ, Masson S, Behera SK, Yamagata T (2008) Extended ENSO predictions using a fully
630 coupled ocean–atmosphere model. J Clim 21:84–93
631 Luo JJ, Zhang R, Behera SK, Masumoto Y, Jin F-F, Lukas R, Yamagata T (2010) Interaction
632 between El Nino and extreme Indian Ocean dipole. J Clim 23:726–742
633 Mayer M, Balmaseda MA, Haimberger L (2018) Unprecedented 2015/2016 Indo-Pacific heat
634 transfer speeds up tropical Pacific heat recharge. Geophys Res Lett 45:3274–3284
635 Meinen CS, McPhaden MJ (2000) Observations of warm water volume changes in the equatorial
636 Pacific and their relationship to El Niño and La Niña. J Clim 13:3551–3559
637 Moorthi S, Pan H-L, Caplan P (2001) Changes to the 2001 NCEP operational MRF/AVN global
638 analysis/forecast system. NWS technical procedures bulletin no. 484, 14 pp.
639 Murtugudde R, Busalacchi AJ (1999) Interannual variability of the dynamics and
640 thermodynamics of the Indian Ocean. J Clim 12:2300–2326
641 Murtugudde R, McCreary J, Busalacchi AJ (2000) Oceanic processes associated with anomalous
642 events in the Indian Ocean with relevance to 1997-98. J Geophys Res 105:3295–3306
643 Okumura YM, Deser C (2010) Asymmetry in the duration of El Niño and La Niña. J Clim
644 23:5826–5843
645 Pacanowski RC, Griffies SM (1998) MOM 3.0 manual. NOAA/GFDL 668 pp
646 Pan H-L, Mahrt L (1987) Interaction between soil hydrology and boundary layer developments.
647 Bound-Layer Meteor 38:185–202
648 Ramesh N, Murtugudde R (2013) All flavors of El Niño have similar subsurface origins. Nature
649 Clim Change 3:42–46
650 Reynolds RW, Rayner NA, Smith TM, Stokes DC, Wang W (2002) An improved in situ and
651 satellite SST analysis for climate. J Clim 15:1609–1625
652 Saha S et al (2006) The NCEP climate forecast system. J Clim 19:3483–3517
653 Saha S et al (2014) The NCEP climate forecast system version 2. J Clim 27:2185–2208
654 Saji NH (2018) The Indian Ocean Dipole. Oxford Research Encyclopedia of Climate Science,
655 doi:10.1093/acrefore/9780190228620.013.619
656 Saji NH, Goswami BN, Vinayachandran PN, Yamagata T (1999) A dipole mode in the tropical
657 Indian Ocean. Nature 401:360–363

Saji NH, Yamagata T (2003a) Possible impacts of Indian Ocean dipole mode events on global climate. Clim Res 25:151–169

Saji NH, Yamagata T (2003b) Structure of SST and surface wind variability during Indian Ocean dipole mode events: COADS observations. J Clim 16:2735–2751

Snedecor GW, Cochran WG (1989) Statistical Methods, 8th edn. Iowa State Univ. Press, p503

Stuecker MA, Timmermann A, Jin F-F, Chikamoto Y, Zhang W, Wittenberg AT, Widiasih E, Zhao S (2017) Revisiting ENSO/Indian Ocean Dipole phase relationships. Geophys Res Lett 44:2481–2492

Tamura T, Koike T, Yamamoto A, Yasukawa A, Kitsuregawa M (2011) Contrasting impacts of the Indian Ocean dipole and ENSO on the tropospheric biennial oscillation. SOLA 7:13–16

Trenberth KE (1997) The definition of El Niño. Bull Amer Meteor Soc 78:2771–2777

Wallace JM, Rasmusson EM, Mitchell TP, Kousky VE, Sarachik ES, von Storch H (1998) On the structure and evolution of ENSO-related climate variability in the tropical Pacific. J Geophys Res 103:14241–14260

Wang DX, Liu QY, Liu Y, Shi P (2004) Connection between interannual variability of the western Pacific and eastern Indian Oceans in the 1997–1998 El Niño event. Prog Nat Sci 14: 423–429

Wang H, Kumar A (2015) Assessing the impact of ENSO on drought in the U.S. Southwest with the NCEP climate model simulations. J Hydrol 526:30–41. doi:10.1016/j.jhydrol.2014. 12. 012

Wang H, Kumar A, Wang W (2013) Characteristics of subsurface ocean response to ENSO assessed from simulations with the NCEP climate forecast system. J Clim 26:8065–8083

Wang H, Kumar A, Wang W, Xue Y (2012a) Seasonality of the Pacific decadal oscillation. J Clim 25:25–38

Wang H, Kumar A, Wang W, Xue Y (2012b) Influence of ENSO on Pacific decadal variability: An analysis based on the NCEP Climate Forecast System. J Clim 25:6136–6151

Wang H, Murtugudde R, Kumar A (2016) Evolution of Indian Ocean dipole and its forcing mechanisms in the absence of ENSO. Clim Dyn 47:2481–2500

687 Wang H, Pan Y, Kumar A, Wang W (2013) Modulation of convectively coupled Kelvin wave
688 activity in the tropical Pacific by ENSO. Acta Meteoro Sinica 27:295–307
689 Weare BC, Nasstrom JS (1982) Examples of extended empirical orthogonal function analysis.
690 Mon Wea Rev 110:481–485
691 Webster PJ, Moore AM, Loschning JP, Leben RR (1999) Coupled ocean-atmosphere dynamics
692 in the Indian Ocean during 1997–98. Nature, 401:356–360
693 Wieners CE, de Ruijter WPM, Ridderinkhof W, von der Heydt AS, Dijkstra HA (2016) Coherent
694 tropical Indo-Pacific interannual climate variability. J Clim 29:4269–4291
695 Wieners CE, Dijkstra HA, de Ruijter WPM (2017a) The influence of the Indian Ocean on ENSO
696 stability and flavor. J Clim 30:2601–2620
697 Wieners CE, Dijkstra HA, de Ruijter WPM (2017b) The influence of atmospheric convection on
698 the interaction between the Indian Ocean and ENSO. J Clim 30:10155–10178
699 Wijffels SE, Meyers GM (2004) An intersection of oceanic wave guides: variability in the
700 Indonesian throughflow region. J Phys Oceanogr 34:1232–1253
701 Wu R, Kirtman BP (2004) Understanding the impacts of the Indian Ocean on ENSO variability
702 in a coupled GCM. J Clim 17:4019–4031
703 Xiao ZN, Yan HM, Li CY (2002) The relationship between Indian Ocean SSTA dipole index
704 and the precipitation and temperature over China. J Tropical Meteor 18:335–344 (**in**
705 **Chinese**)
706 Xie S-P, Hu K, Hafner J, Tokinaga H, Du Y, Huang G, Sampe T (2009) Indian Ocean capacitor
707 effect on Indo-Western Pacific climate during the summer following El Niño. J Clim
708 22:730–747
709 Zhou Q, Duan W, Mu M, Feng R (2015) Influence of positive and negative Indian Ocean dipoles
710 on ENSO via the Indonesian Throughflow: Results from sensitivity experiments. Adv
711 Atmos Sci 32:783–793
712

713 **Table 1** Number of SON seasons and percentage of co-occurrence for different phases of IOD
714 and ENSO. Both ENSO and IOD events are defined using their corresponding standard
715 deviation of the 480-year SON time series. Please see the main text for details.

Co-occurrence	Number of SON Seasons	Percentage of Co-occurrence
Positive IOD & El Niño	29	27% (29 out of 108)
Negative IOD & La Niña	35	39% (35 out of 90)
Positive IOD & La Niña	5	5% (5 out of /108)
Negative IOD & El Niño	4	4% (4 out of 90)

716

717

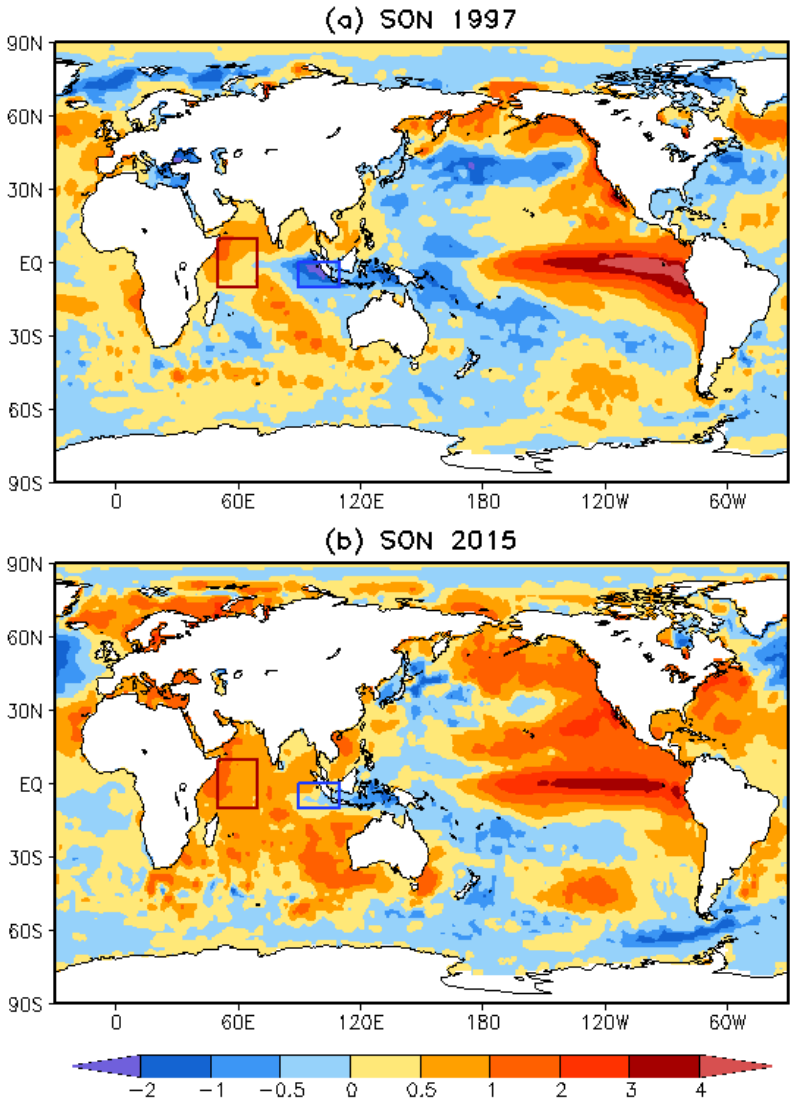

718

719 **Fig. 1** Distribution of seasonal mean SST anomaly (K) in (**a**) SON 1997 and (**b**) SON 2015. The
720 red and blue boxes denote the domains of WIO (50°–70°E, 10°S–10°N) and EIO (90°–110°E,
721 10°S–Eq.) used for averaging SST anomalies for the IOD index.
722

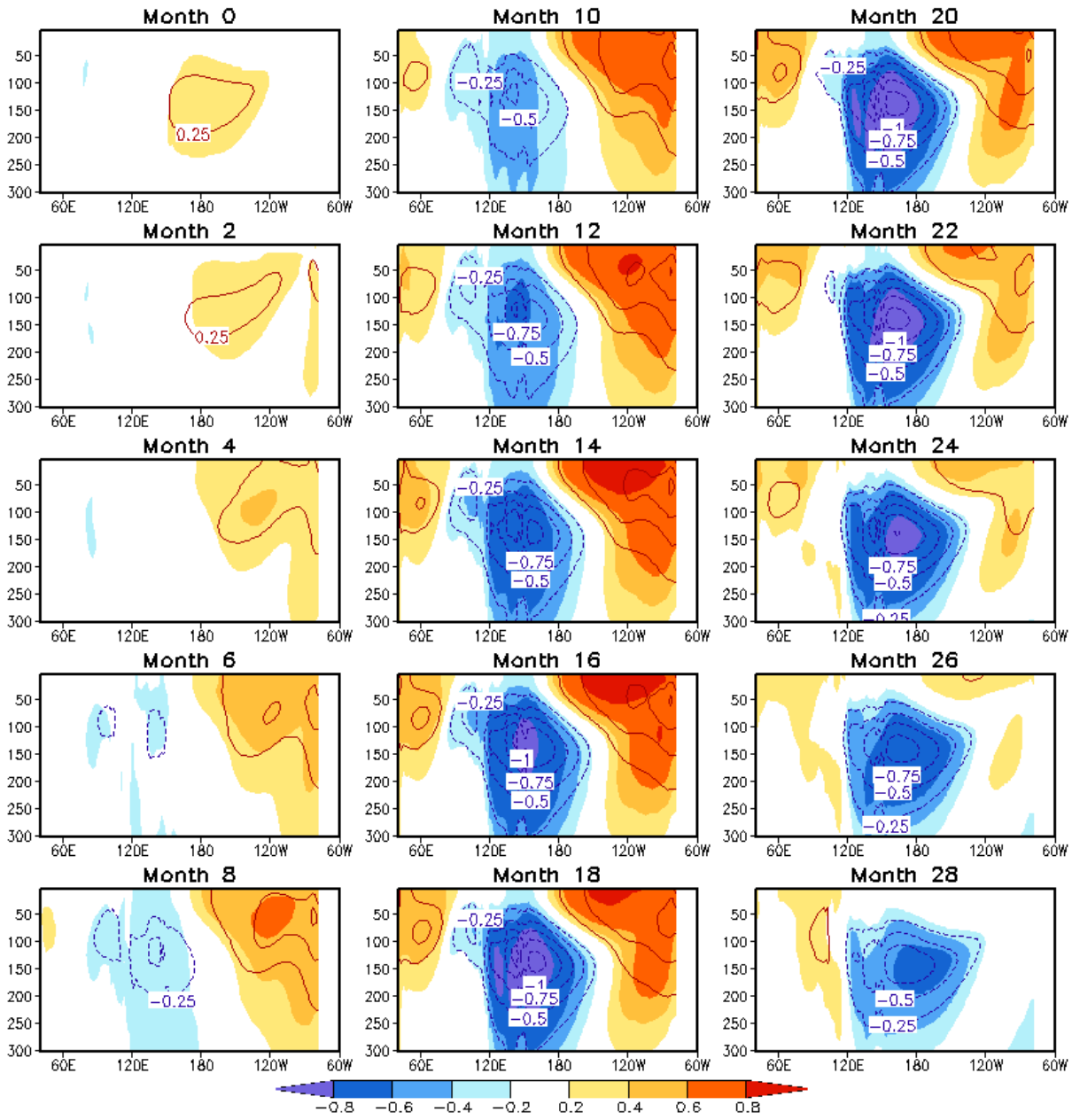

723

724 **Fig. 2** Correlation (shading) and regression (contour) coefficients of monthly mean ocean
725 temperature averaged over 10ºS–5ºN against the PC time series of the first EEOF from month 0
726 to month 28. Month 28 denotes ocean temperature lagging PC1 by 28 months. Contour interval
727 is 0.25 K with negative values dashed and zero contours omitted. Correlations exceeding ±0.2
728 with shadings are above the 99% significance level, estimated by the two-tailed t-test (Snedecor
729 and Cochran 1989).
730

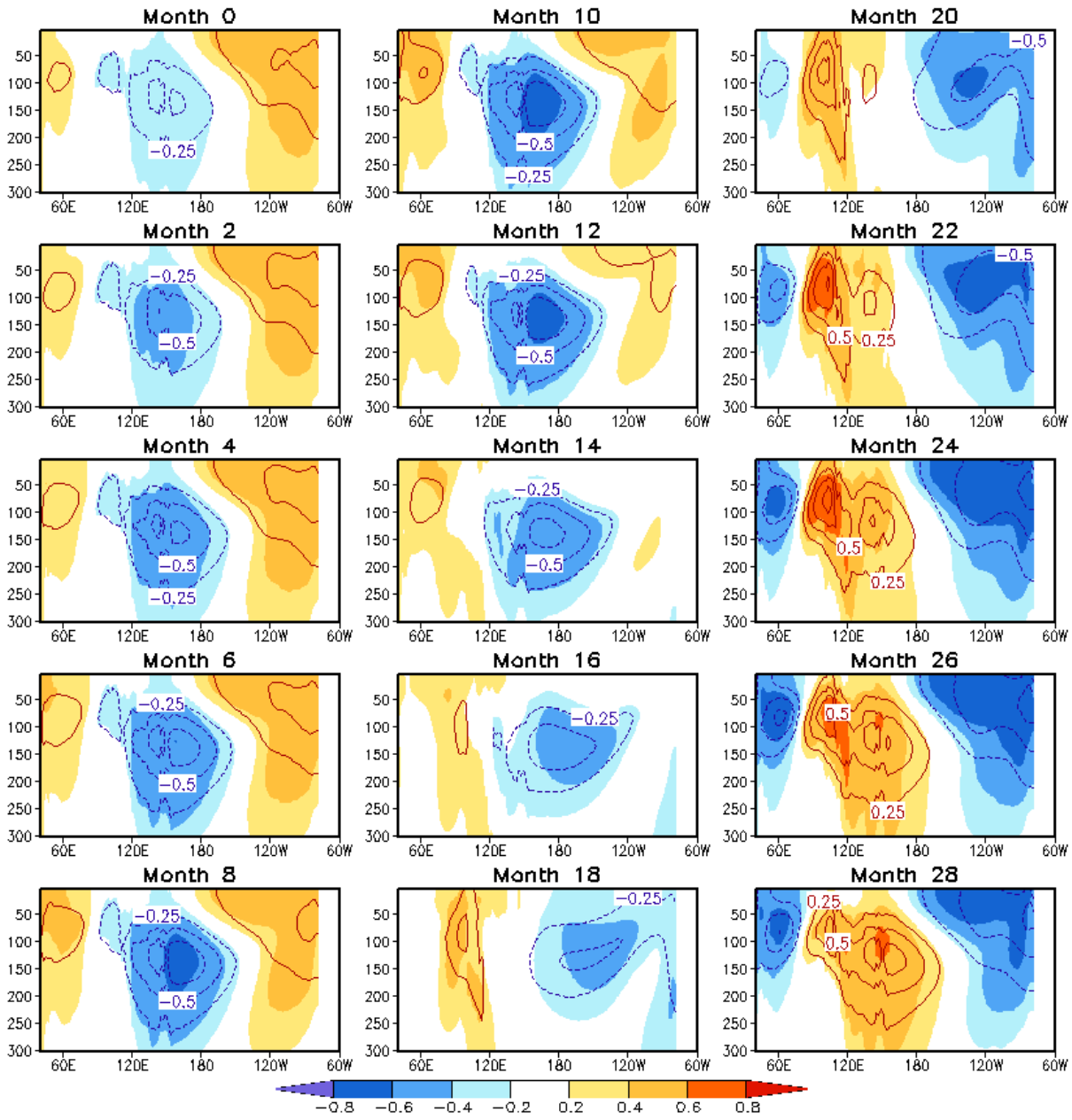

731

732 **Fig. 3** Same as Fig. 2 but for the second EEOF.

733

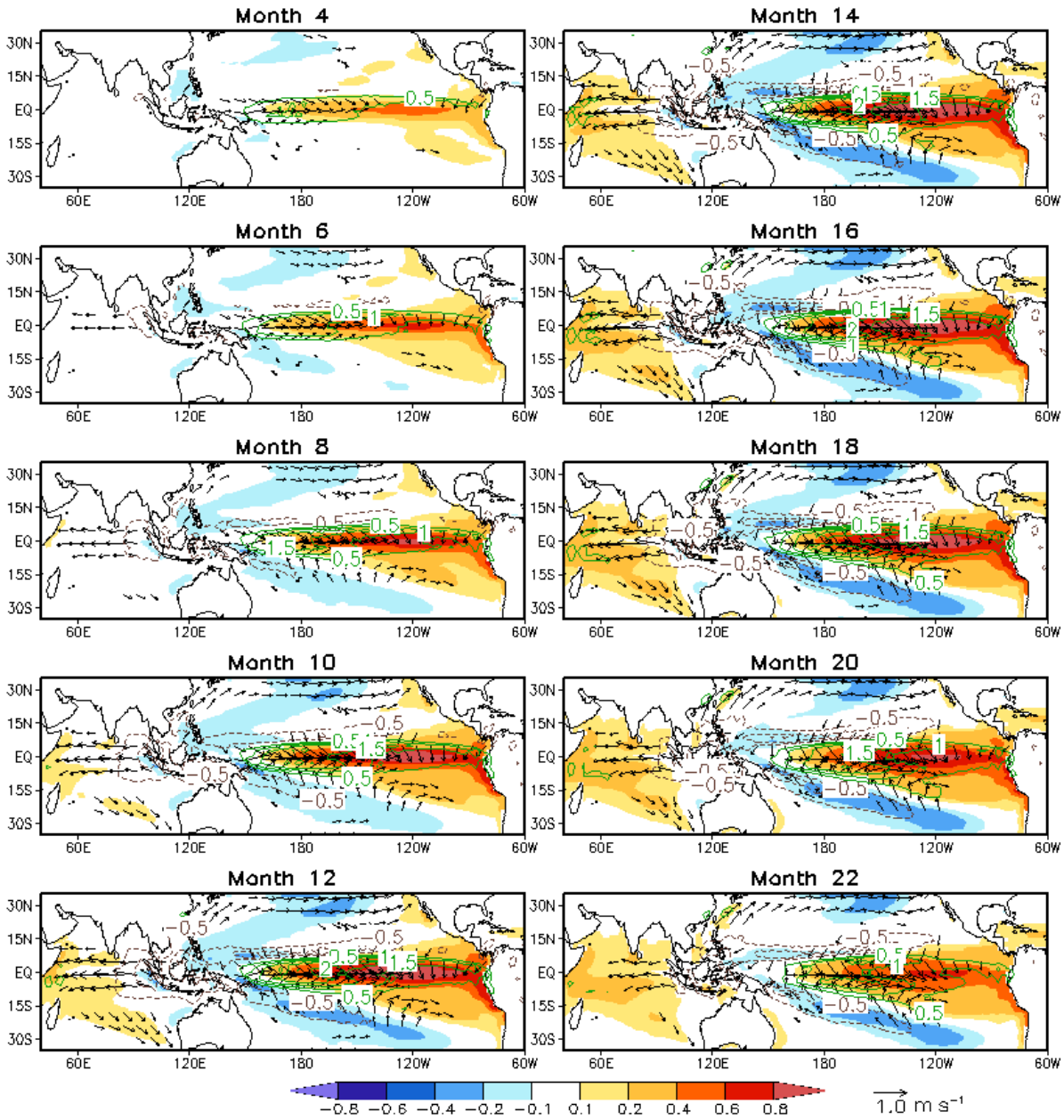

734

735 **Fig. 4** SST (shading, K), 10-m wind (vector, m s^{-1}), and precipitation (contour, mm day^{-1})
736 anomalies associated with a one-standard-deviation departure in the PC1 time series obtained by
737 regressing 480-year monthly fields against the time series of EEOF1 in the ENSO run from
738 month 4 to month 22. Contour interval is 0.5 mm day^{-1} with green for positive values, dark
739 brown for negative values (dashed), and zero contours omitted. Wind anomalies are plotted only
740 over the oceans with anomalous wind speeds larger than 0.25 m s^{-1}.
741

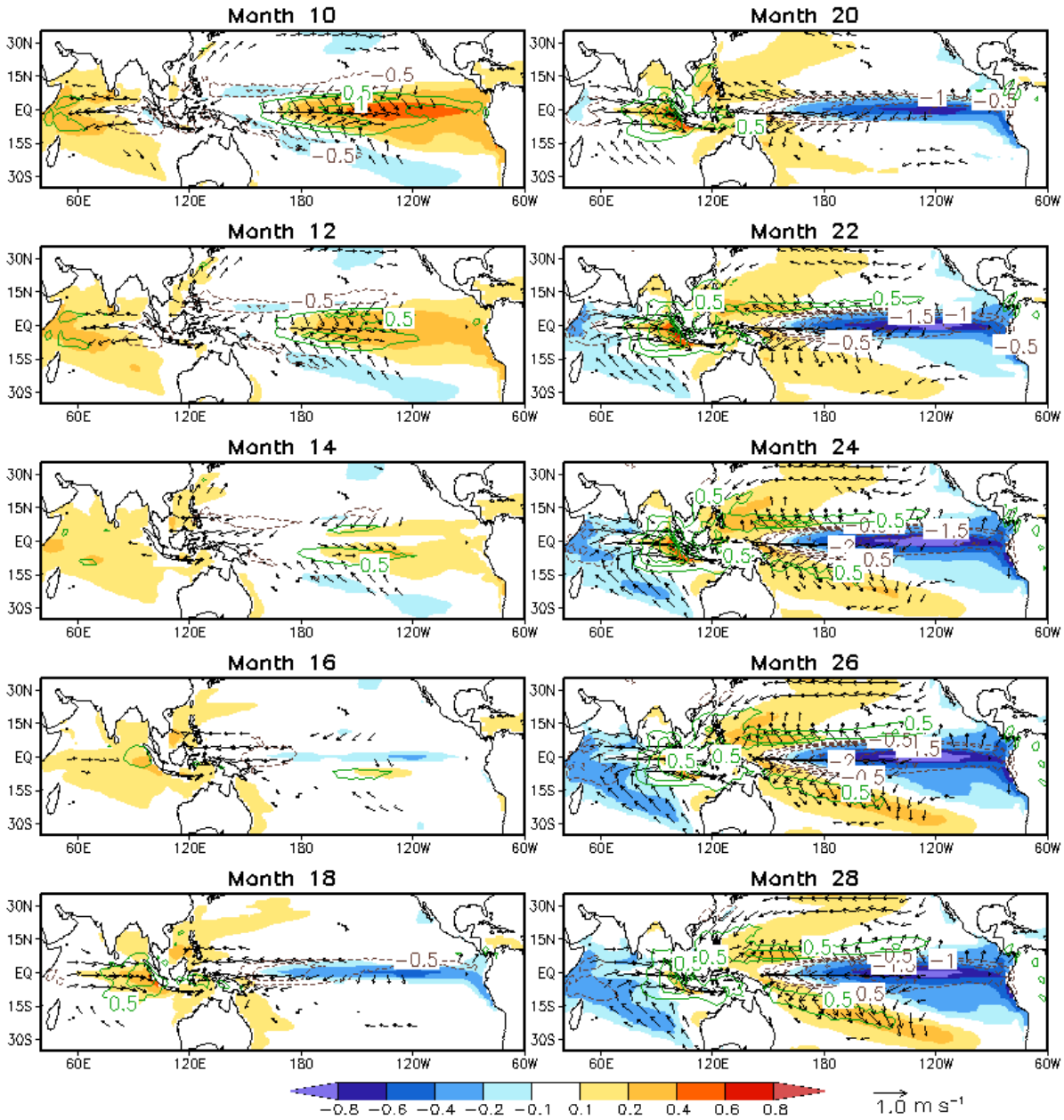

Fig. 5 Same as Fig. 4 but for the second EEOF from month 10 to month 28.

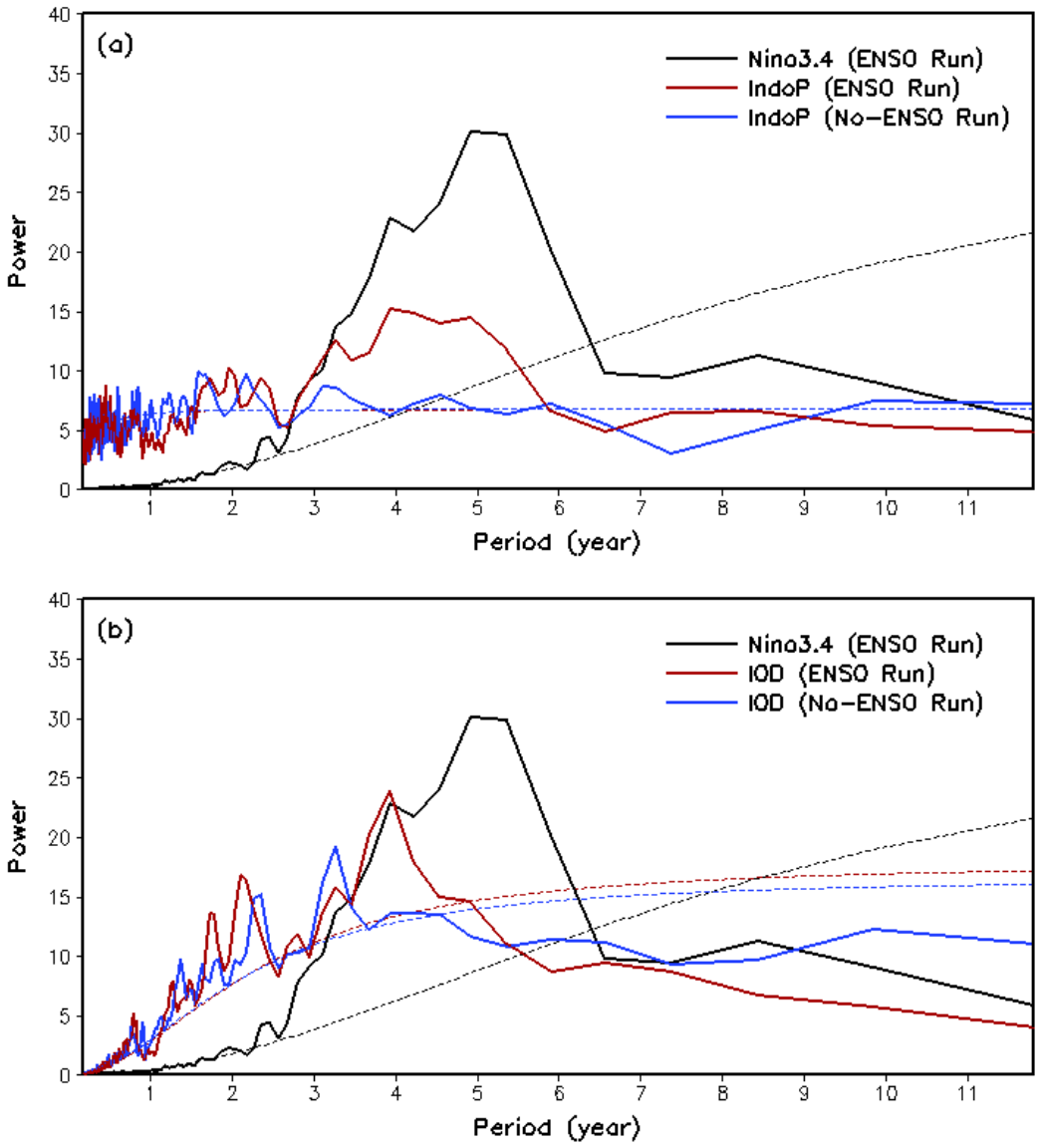

745

746 **Fig. 6** Power spectra of the normalized 480-year time series of (**a**) the Niño 3.4 index in the
747 ENSO run (black) and the IndoP index in the ENSO run (red) and no-ENSO run (blue), and (**b**)
748 the Niño 3.4 index in the ENSO run (black) and the IOD index in the ENSO run (red) and no-
749 ENSO run (blue). Dashed lines are corresponding red-noise spectra. The power spectra are
750 averages over eight 60-year segments. The power spectra of the IndoP index and the IOD index
751 are multiplied by a factor of 5 and 2, respectively, for display purposes only.

752

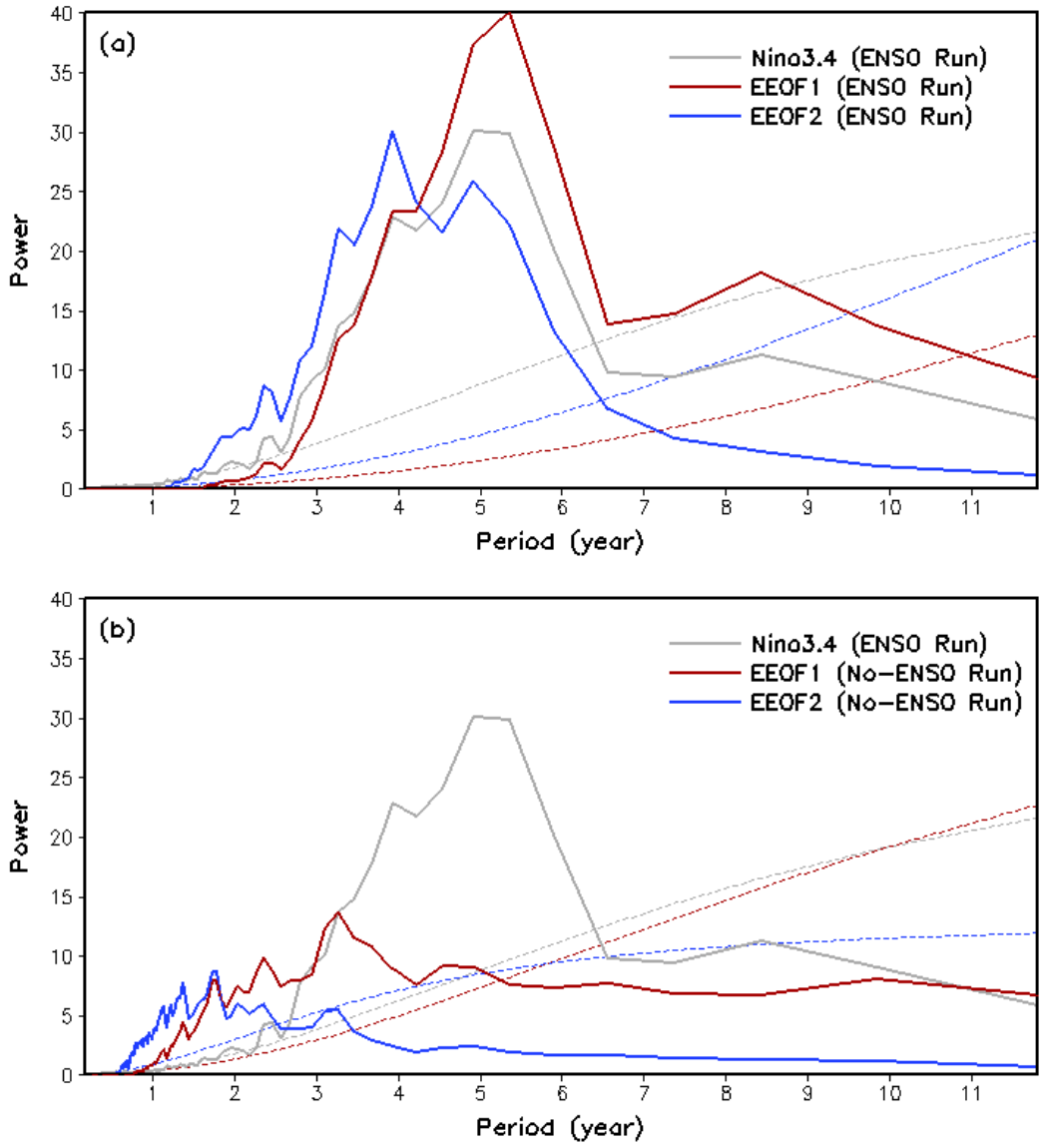

753

754 **Fig. 7** Power spectra of the normalized 480-year time series of (**a**) the Niño 3.4 index in the
755 ENSO run (grey) and the PCs of EEOF1 (red) and EEOF2 (blue) in the ENSO run and (**b**) in the
756 no-ENSO run. Dashed lines are corresponding red-noise spectra. The power spectra are the
757 averages over eight 60-year segments.
758

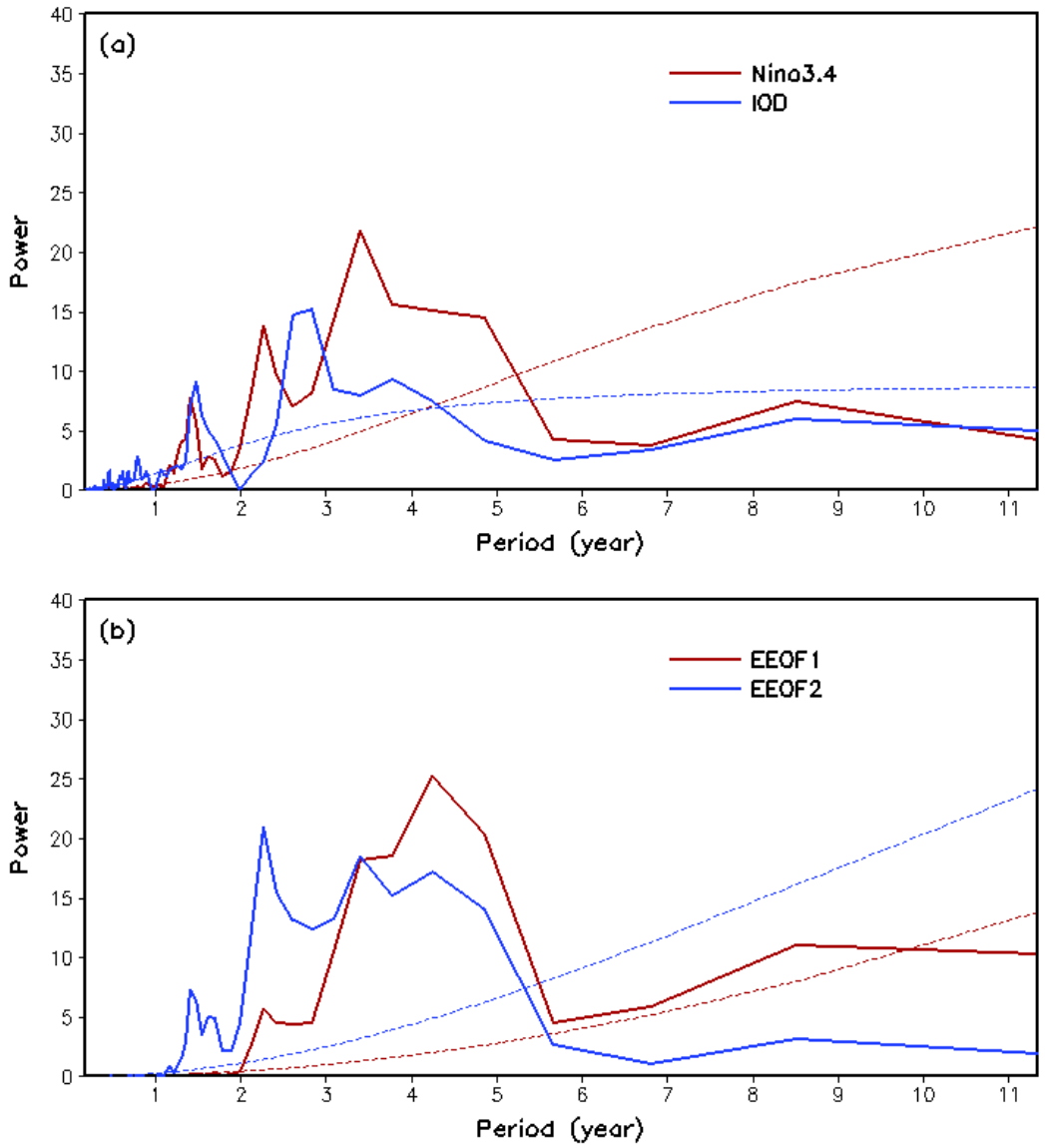

759

760 **Fig. 8** Power spectra of the normalized 36-year time series of (**a**) the Niño 3.4 index and the IOD
761 index and (**b**) the PCs of EEOF1 (red) and EEOF2 (blue) in GODAS. Dashed lines are
762 corresponding red-noise spectra.
763

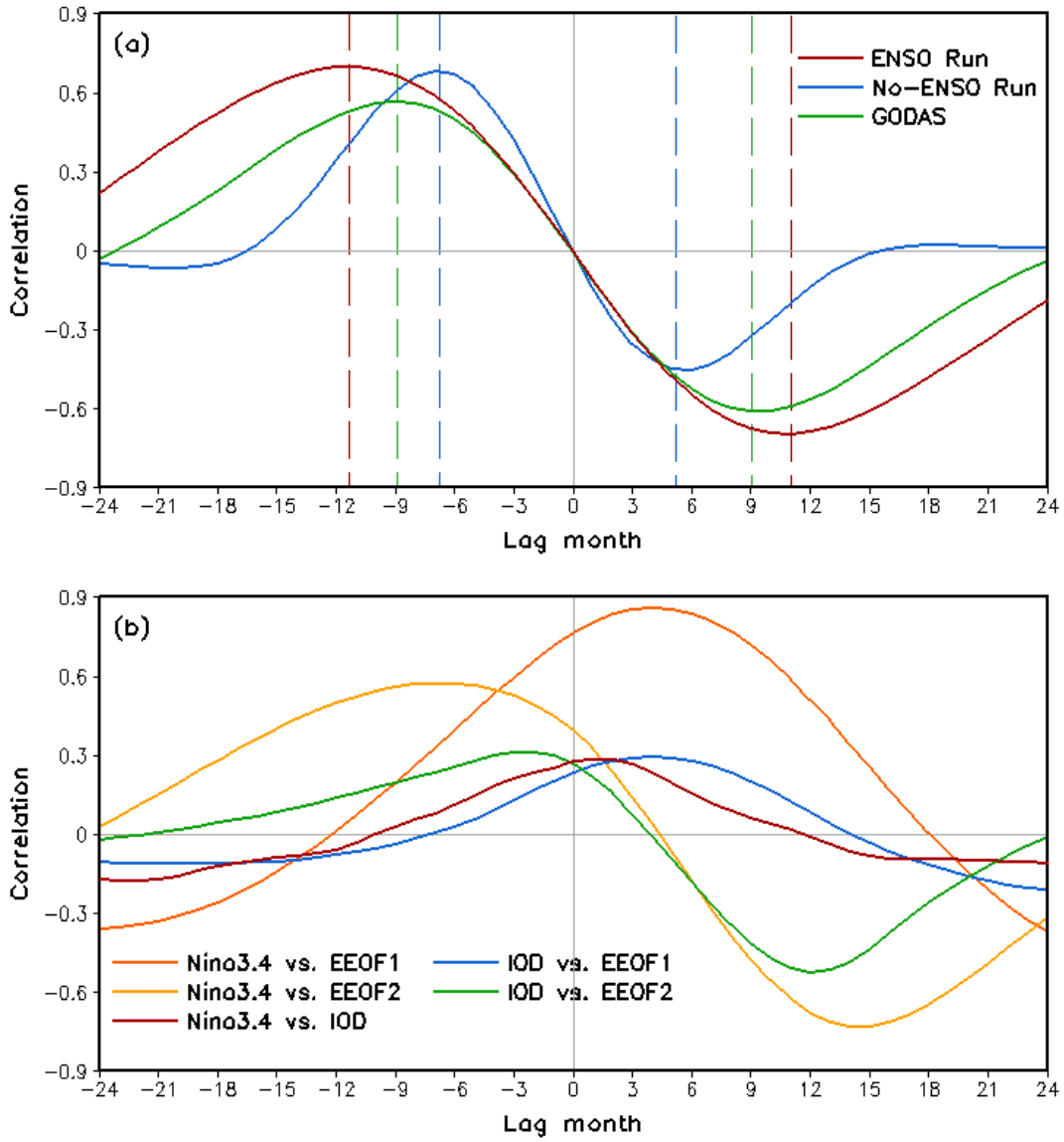

764

765 **Fig. 9** (**a**) Lead and lag correlations between the two PC time series of EEOF1 and EEOF2 in the
766 ENSO run (red solid line), no-ENSO run (blue solid line), and GODAS (green solid line) for
767 EEOF1 leading EEOF2 24 months (lag month = –24) to EEOF1 lagging EEOF2 24 months (lag
768 month = 24), and (**b**) similar lead and lag correlations of the Nino 3.4 index with the two PC time
769 series of EEOF 1 (orange) and EEOF2 (yellow), the IOD index with the two PC time series of
770 EEOF1 (blue) and EEOF2 (green), and the Nino 3.4 index with the IOD index (red) in the ENSO
771 run from lag month –24 to lag month 24, namely, from the Nino 3.4 index leading the IOD index
772 24 months to lagging 24 months, for example. Vertical dashed color lines in (**a**) denote the lag
773 month of the largest positive and negative correlation coefficients.
774

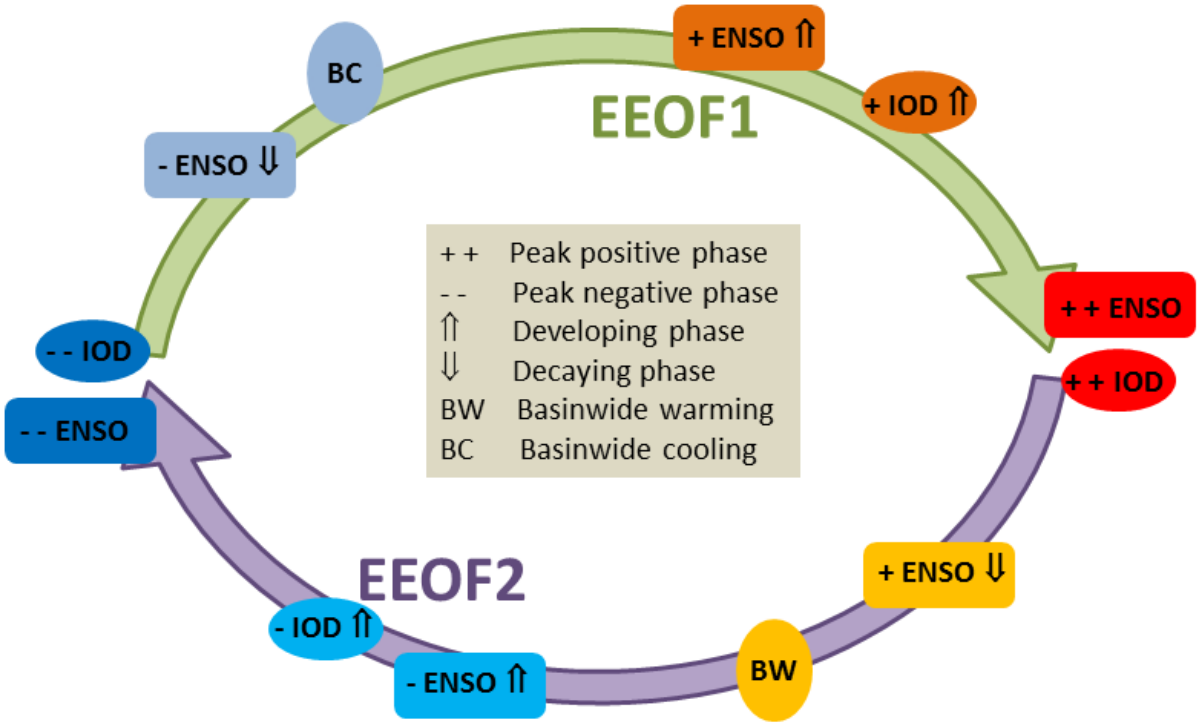

775
776 **Fig. 10** Schematic of the covariations of ENSO and IOD through the alternation between EEOF1
777 and EEOF2. Signs + and – denote evolutionary phases.
778

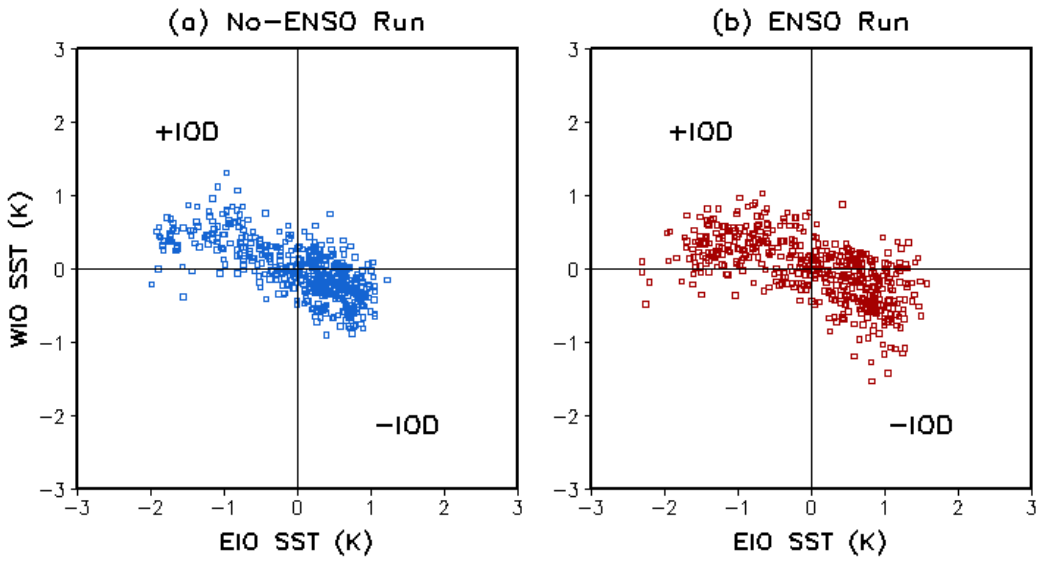

779

780 **Fig. 11** Scatter plot of 480-year EIO SST versus WIO SST in SON for (**a**) the no-ENSO run and
781 (**b**) the ENSO run.

782

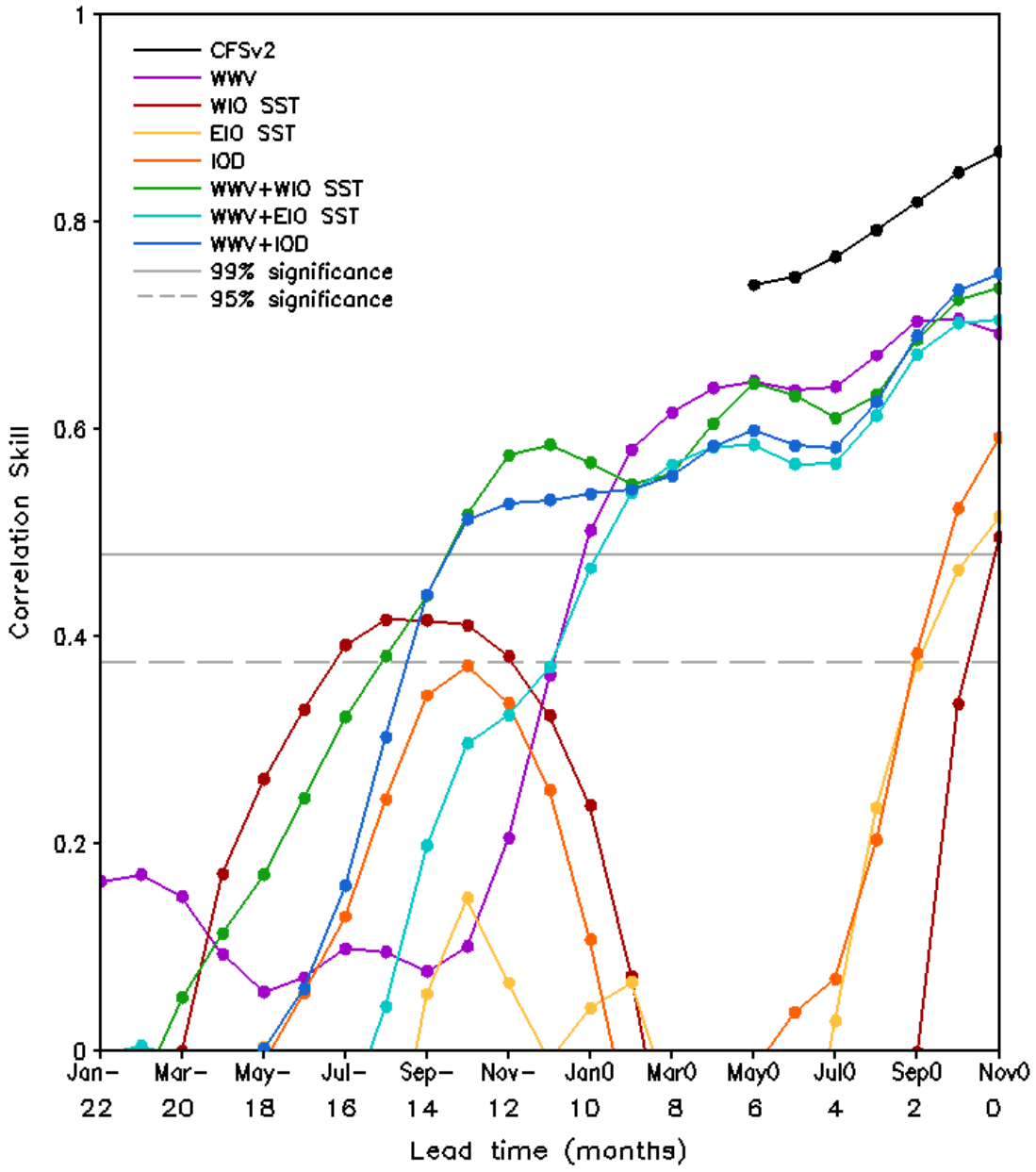

783

784 **Fig. 12** Anomaly correlation skills of CFSv2 dynamical forecast (black) and statistical forecasts
785 using one predictor (purple for WWV, red for WIO SST, yellow for EIO SST, orange for IOD
786 index) and two predictors (green for WWV + WIO SST, cyan for WWV + EIO SST, blue for
787 WWV + IOD) for DJF Niño 3.4 SST with lead times from 22 months to 0 month, corresponding
788 to forecasts made from January of previous year to November of current year (Jan– to Nov0 with
789 – and 0 for previous year and current year, respectively). Solid (dash) gray line denotes the
790 threshold of the anomaly correlation at the 99% (95%) significance level.

791

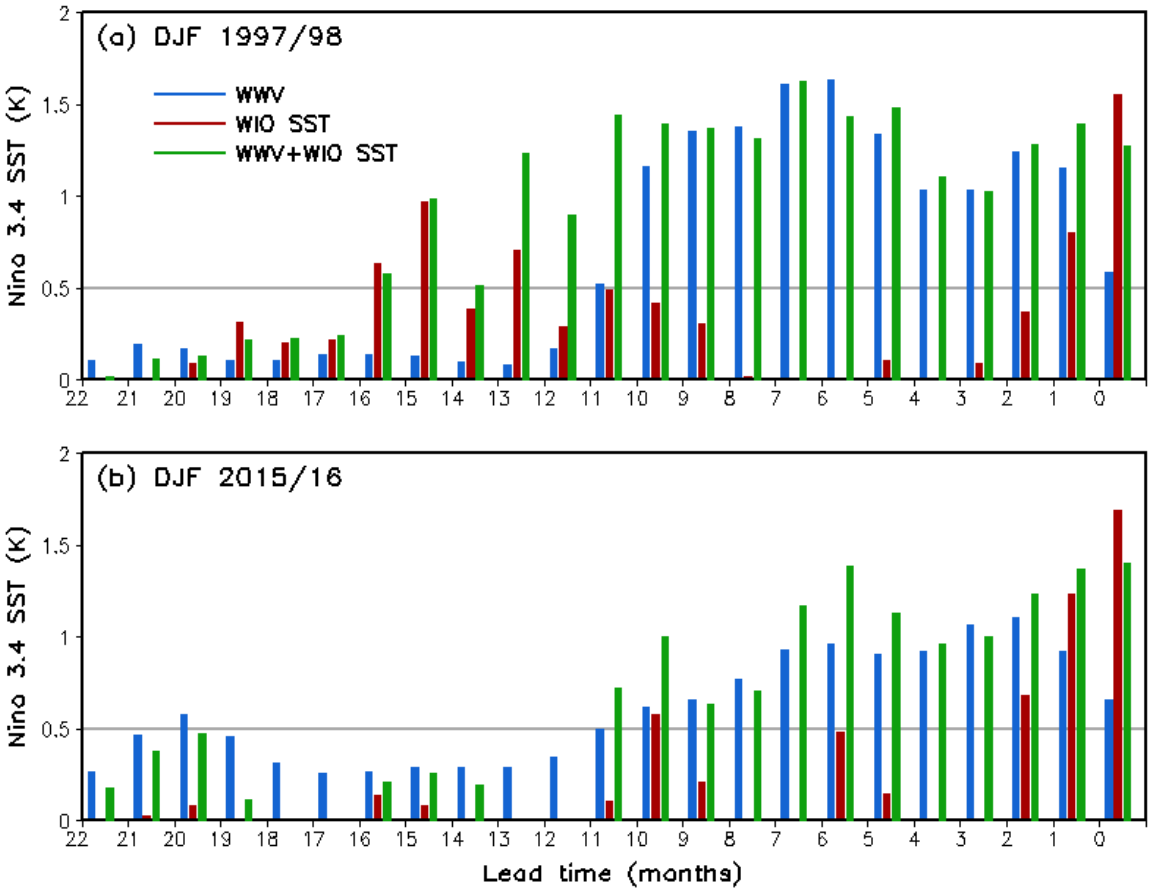

792

793 **Fig. 13** Niño 3.4 SST anomalies (K) of (**a**) DJF 1997/98 and (**b**) DJF 2015/16 predicted by the
794 linear regression model using one predictor (blue for WWV; red for WIO SST) and two
795 predictors (WWV + WIO SST, green) with lead times from 22 months to 0 month. Gray line
796 denotes the threshold (0.5 K) of the Niño 3.4 index for an El Niño.

797

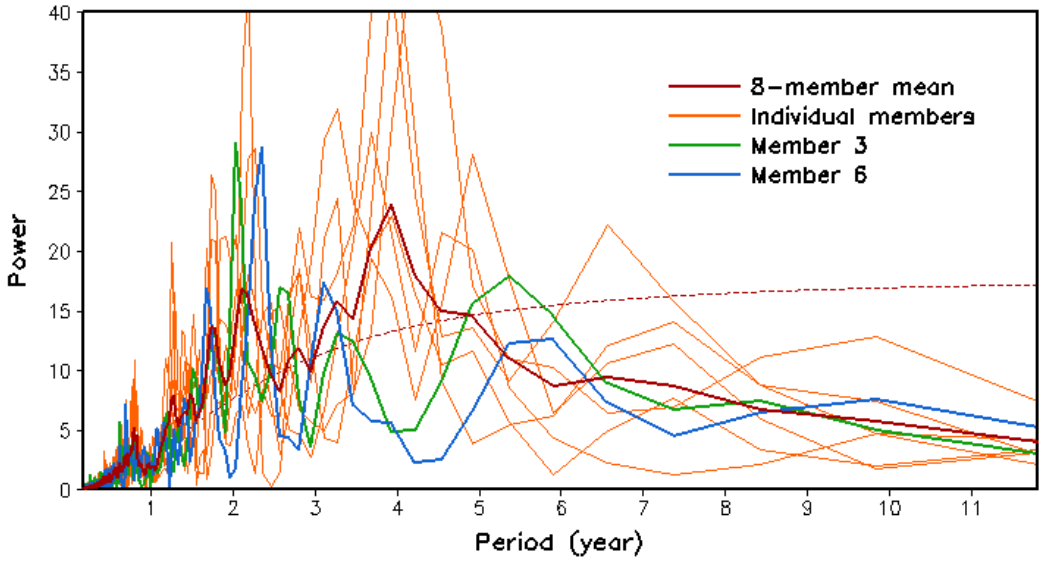

Fig. A1 Power spectra of the normalized 480-year time series of the IOD index in the ENSO run (red), which is the averages over eight 60-year segments, and those of eight individual 60-year segments (6 orange, 1 green, and 1 blue). Dashed line is the red-noise spectra.